International Journal of Heat and Mass Transfer 135 (2019) 569–590

Contents lists available at ScienceDirect

International Journal of Heat and Mass Transfer

journal homepage: www.elsevier.com/locate/ijhmt

Identification of condensation flow regime at different orientations using temperature and pressure measurements

Lucas E. O'Neill [a], R. Balasubramaniam [b], Henry K. Nahra [b], Mohammad M. Hasan [b], Jeffrey R. Mackey [c], Issam Mudawar [a,*]

[a] Purdue University Boiling and Two-Phase Flow Laboratory (PU-BTPFL), School of Mechanical Engineering, Purdue University, 585 Purdue Mall, West Lafayette, IN 47907, USA
[b] NASA Glenn Research Center, 21000 Brookpark Road, Cleveland, OH 44135, USA
[c] Vantage Partners, 3000 Aerospace Parkway, Brook Park, OH 44142, USA

ARTICLE INFO

Article history:
Received 11 November 2018
Received in revised form 23 January 2019
Accepted 28 January 2019
Available online 12 February 2019

Keywords:
Flow condensation
Flow regime determination
Flow regime maps
Orientation effects

ABSTRACT

While many prior works in the field relied upon direct optical access to determine condensation flow regimes, the present work outlines a new methodology utilizing temperature and pressure measurements to identify condensation flow regimes. For vertical upflow condensation, amplitude of dynamic temperature and pressure oscillations are shown to clearly indicate transition from counter-current flow regimes (*i.e., falling film*, *oscillating film*, *flooding*) to annular, co-current flow (*climbing film* flow regime). In horizontal flow condensation, standard deviation between multiple thermocouple measurements distributed around the tube circumference was calculated at all axial (stream-wise) measurement locations. High values of standard deviation are present for stratified flow (*stratified flow, wavy-stratified, plug flow*), while axisymmetric flow regimes (*i.e., slug flow*, *annular flow*) yield significantly lower values. Successful development of this technique represents a valuable contribution to literature as it allows condensation flow regime to be identified without the often-costly restriction of designing a test section to allow optical access. Identified flow regimes in both vertical upflow and horizontal flow orientations are compared to regime maps commonly found in the literature in pursuit of optimum performing maps.

© 2019 Elsevier Ltd. All rights reserved.

1. Introduction

1.1. Flow condensation as an enabling technology for phase change thermal management

Due to their high heat transfer coefficients, phase change heat transfer processes play an important role in industries ranging from high flux thermal management, to nuclear power generation, to commercial and residential HVAC&R [1]. Work in the field has focused primarily on heat acquisition through boiling and evaporation, as this portion of system design is commonly required to conform to specific dimensions associated with the device from which heat is being acquired, necessitating a detailed understanding of heat transfer mechanisms and accurate design tools. The reciprocal process of condensation, however, has attracted less attention due the relatively fewer constraints imposed on this portion of the system in many traditional ground-based applications.

Advances in sophistication of equipment and scope of missions has led to the consideration of phase change processes as candidates for thermal management and energy transport systems operating in microgravity, where overall system volume and mass limitations drive design decisions to a much higher degree than in ground-based systems. Key targets for application of phase change driven technologies in space include Thermal Control Systems (TCSs), which control temperature and humidity of the operating environment, heat receiver and rejection systems for power generating units, and Fission Power Systems (FPSs), which are projected to provide high power as well as low mass to power ratio [2–4]. Regardless of specific application, any adoption of phase change technology in microgravity will necessitate a thorough understanding of not only boiling but also condensation heat transfer to ensure system design meets all operating requirements while minimizing both mass and volume.

Many prior studies by researchers at the Purdue University Boiling and Two-Phase Flow Laboratory (PU-BTPFL) and other organizations have investigated both flow boiling and flow condensation in a variety of configurations. For boiling, these include pool boiling [5,6], flow boiling in macro- [7–12] and micro-channels

* Corresponding author.
E-mail address: mudawar@ecn.purdue.edu (I. Mudawar).
URL: https://engineering.purdue.edu/BTPFL (I. Mudawar).

https://doi.org/10.1016/j.ijheatmasstransfer.2019.01.133
0017-9310/© 2019 Elsevier Ltd. All rights reserved.

Nomenclature

C	Wallis parameter
c_p	specific heat at constant pressure
D	diameter
Fr	Froude number
G	mass velocity
g	Earth's gravitational constant
h_{fg}	latent heat of vaporization
j	superficial velocity
$\dot{m}$	mass flowrate
N	number of samples
P	pressure
P'	amplitude of pressure fluctuations
Pwr	power input
Q_{cond}	total condensation energy transfer in test section
Re	Reynolds number
S_2	flow transition parameter
T	temperature
T'	amplitude of temperature fluctuations
t	time
We	Weber number
X_{tt}	Lockhart-Martinelli parameter
x_e	thermodynamic equilibrium quality
z	streamwise position

Greek Symbol

Γ	liquid film mass flowrate
φ	two-phase multiplier
μ	dynamic viscosity
ρ	density
σ	surface tension; standard deviation

Subscripts

0-n	indicates a time span ($t = 0$ to $t = n$) over which an average or max is found
ave	average
BH	bulk heater
f	saturated liquid
film	referring to condensate liquid film
FC	FC-72, condensate
g	saturated vapor
H2O	water, cooling fluid
i	inner (refers to diameter)
in	inlet to condensation length (refers to condensate)
max	max value over the range evaluated
mean	mean value over the range evaluated
o	outer (refers to diameter)
out	outlet to condensation length (refers to condensate)
SS	stainless-steel (inner condensation tube)

Acronyms

CM-FV	condensation module for flow visualization
CM-HT	condensation module for heat transfer

[13–19], jet impingement [20,21], spray cooling [22–26], and hybrid schemes involving multiple approaches [27]. Condensation configurations including falling film [28–30], flow through single mini-channels [31–38], flow through parallel micro-channel arrays [39–44], and dropwise condensation [45–47] have also been studied. Although both boiling and condensation processes are important to design of systems utilizing phase change heat transfer, the present work will focus on flow condensation in smooth, circular tubes, as this is a commonly employed configuration.

One key aspect of flow condensation often underemphasized is the need to accurately determine condensation flow regime. Flow regimes are used to classify flow conditions based on distribution of liquid and vapor within the condensation length. This distribution has a significant impact on local heat transfer, meaning accurate identification and prediction of flow regime is paramount to system design and interpretation of observed behavior.

1.2. Predictive tools for condensation flow regime

Many prior studies in the field have devoted significant effort to identifying two-phase flow regimes and developing tools for their prediction. In vertical downflow orientation, where body force acts to stabilize the flow by ensuring liquid phase flows along with vapor and out of the channel, regime maps are considered largely unnecessary as flow is always axisymmetric and co-current. In vertical upflow, horizontal, and intermediate flow angles, however, the relative magnitude of body force to flow inertia is critical to determining both motion and position of liquid phase within the condensation length.

One of the earliest studies to focus on flow regime in vertical tubes by Wallis [48] provided a method for predicting flooding velocities (*i.e.,* velocities at which liquid phase will remain largely stationary while vapor phase continues to flow) for adiabatic mixtures of water and air in vertical upflow orientation. His work paved the way for development of flow regime maps for vertical upflow by future researchers [35], who expanded his analysis to provide regime transition criteria for *falling film*, *flooding*, *oscillating film*, and *climbing film* flow regimes.

Investigation into flow regimes for horizontal flows has been far more prolific than vertical flows. One of the most commonly cited works is that of Taitel and Dukler [49] who developed flow regime transition criteria (and thus a flow regime map) for horizontal, adiabatic two-phase flows. They utilized the air-water data of Mandhane et al. [50] to validate their map.

Although developed for adiabatic two-phase flows, Breber et al. [51] showed the map of Taitel and Dukler [49] provided good prediction for flow regime in condensing flows as well. They then provided a simplified method for flow regime prediction based on that of Taitel and Dukler. This basic form was again leveraged when Tandon et al. [52] provided a modified version of Breber et al.'s map [51].

A slightly different approach to modeling flow regime transitions was taken by Soliman [53,54], who modeled transitions from *annular flow* to *wavy flow* and *mist flow* to *annular flow* in separate studies. Similar to Wallis in vertical upflow [58], Soliman's approach has been adapted in recent studies to provide predictions of many additional flow regimes in horizontal flow, including *stratified flow*, *wavy-stratified flow*, *wavy-annular flow with gravity influence*, *wavy-annular flow without gravity influence*, *slug flow,* and others (depending on test geometry) [36,40,55].

In addition to these, recent years have seen a significant increase in the number of flow transition criteria (and associated flow regime maps) available for use in the literature. Notable works include those of Cavallini et al. [56], Wang et al. [57], Hajal et al. [58], Coleman and Garimella [59], and Song et al. [60].

In addition to this, almost all works presenting flow condensation heat transfer results provide some discussion on observed and/or predicted flow regime.

Historically, all investigation of condensation flow regime has been done through direct (optical) observation of liquid film distribution within the flow channel. This typically requires compromises to be made during test section design, as providing an optically transparent region for direct image capture often eliminates the option of gathering detailed heat transfer data for that portion of the module. Liebenberg et al. attempted some characterization of flow regime based on power spectral density of pressure fluctuations during condensation in both smooth and enhanced tubes [61,62], but ultimately relied upon images for determination of flow regime.

The present work aims to present a new method for identifying flow regime in both horizontal and vertical flows using only temperature and pressure data. Although not as comprehensive as direct visualization of flow behavior, it allows interpretation of heat transfer behavior and heat exchanger performance based on observed flow regime without the necessity of optical transparency within the condensation length. This is particularly useful in industrial applications, as temperature and pressure monitoring are commonly available but optical access rarely is. It will also be very helpful in interpreting flow condensation heat transfer data gathered on the International Space Station (ISS) as part of NASA's Flow Boiling and Condensation Experiment in the absence of direct visualization behavior.

1.3. Objectives of study

The present study is part of NASA's Flow Boiling and Condensation Experiment (FBCE), an ongoing collaboration between NASA Glenn Research Center and the Purdue University Boiling and Two-Phase Flow Laboratory (PU-BTPFL) with the goal of developing an experimental facility for the International Space Station (ISS) capable of gathering long term flow boiling and flow condensation data in a microgravity environment. A summary of scientific developments realized as a part of the project can be found in the recent review article prepared by Mudawar [63], including details of extensive microgravity flow boiling testing performed during parabolic flights [64–66].

This work deals with the condensation portion of FBCE and augments prior work dealing with 1-g and parabolic flight testing [67,68], development of criteria for assessing the influence of body force on flow condensation heat transfer [69,70], computational prediction of flow condensation [71,72], experimental investigation of flow condensation dynamic behavior [73], and correlation of pressure drop and heat transfer coefficient for condensing flows using a large database from available literature [74,75] with presentation of a new method for flow regime identification. Several reviews have also been prepared evaluating semi-empirical and computational approaches for prediction of critical condensation design parameters [76–78].

Key goals for the present work are:

(1) Qualitatively present the competing influences of body force and flow inertia on condensate liquid film behavior using select flow visualization image sequences.
(2) Present new methods for determining flow regime in horizontal and vertical upflow orientations using only temperature and pressure measurements.
(3) Provide validation of new flow regime identification methodology through comparison with flow regime predictions from popular regime maps available in the literature.

It should be noted that the present work is the companion to another study [79] presenting flow condensation heat transfer data reduction, experimental trends, and correlation evaluation using the present dataset. The work presented here outlining identification of flow regimes is referenced throughout the companion study as flow regime is a strongly related to trends in observed heat transfer coefficient.

2. Experimental methods

In order to perform detailed condensation heat transfer measurements in a commonly employed heat exchanger configuration (tube-in-tube counterflow), simultaneous acquisition of flow visualization image sequences was not possible. To overcome this limitation the present study employs two test sections, one designed for heat transfer measurements (Condensation Module for Heat Transfer measurements, CM-HT), and one for capture of flow visualization image sequences (Condensation Module for Flow Visualization, CM-FV). These modules are described in the following subsections.

2.1. Condensation module for heat transfer measurements (CM-HT)

Both modules are constructed as tube-in-tube counterflow heat exchangers, with the inner tube made of stainless steel and the outer annular region machined from transparent polycarbonate plates. In the case of the condensation module for heat transfer (CM-HT), Fig. 1(a) shows the condensate (dielectric FC-72) flows through the inner stainless-steel tube, while the cooling fluid (water) flows through the outer annulus. The inner tube possess an i.d. of 7.12 mm, a wall thickness of 0.41-mm, and the outer annular region has a diameter of 12.70-mm. Both fluid streams possess adiabatic development inlet and exit lengths to eliminate any impact of flow development on condensation heat transfer. Direct measurement of both FC-72 and water inlet and exit temperatures and pressures are made in these adiabatic regions using type-T thermocouples and STS absolute pressure transducers, respectively. Fig. 1(a) shows these measurements are made at the same locations just before and after the condensation length, respectively, although they are slightly offset from one another within the adiabatic lengths.

Fig. 1(a) shows the total condensation length of CM-HT is 574.55 mm. Along the condensation length, both water and stainless-steel surface temperature measurements are made at 11 locations, with minimum spacing (25.4 mm) between measurement stations in the upstream region to facilitate capture of heat transfer information where liquid film is thinnest and changes rapidly, while stations in the downstream region are further apart (up to 88.9 mm). Each axial measurement station (of the 11 total) consists of two type-T thermocouples inserted directly into water flow 180° apart and three type-T thermocouples brazed to the outer surface of the stainless-steel tube 120° apart. The inclusion of multiple, circumferentially spaced thermocouples at each axial measurement station allows determination of flow symmetry, information which will be discussed at length in following sections.

2.2. Condensation module for flow visualization (CM-FV)

Fig. 1(b) shows the condensation module for flow visualization (CM-FV) which, unlike CM-HT, has FC-72 condensing along the outside of the stainless-steel tube, while cooling water flows through the inner stainless-steel tube. This is done to allow direct visual access to the condensate film, further facilitated by the polycarbonate channel possessing rectangular walls instead of the

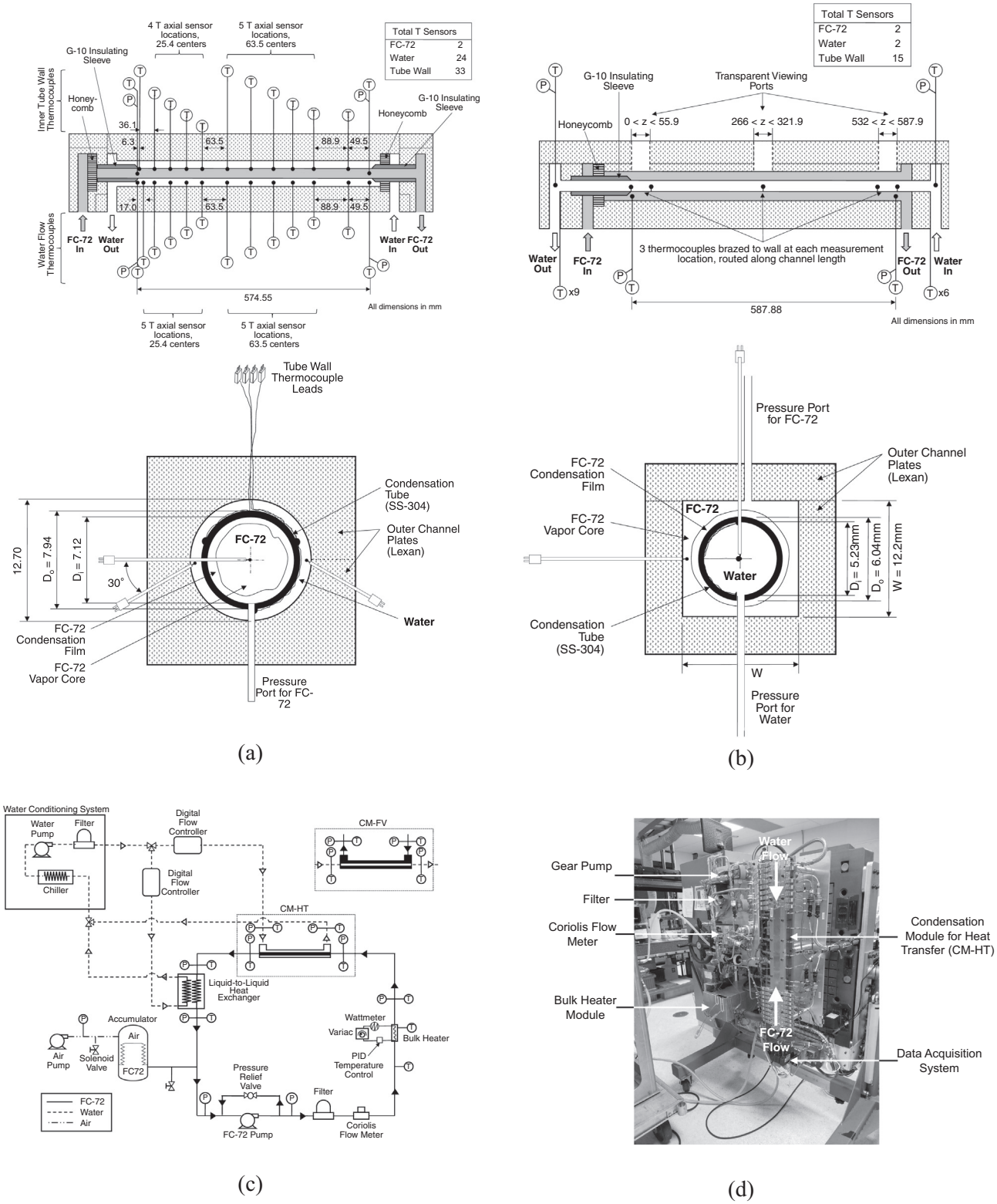

Fig. 1. (a) Condensation Module for Heat Transfer measurements (CM-HT) schematics, (b) Condensation Module for Flow Visualization (CM-FV) schematics, (c) flow loop schematic, and (d) facility photo.

circular path provided in CM-HT (eliminating the need to image through a curved interface). Although condensation along the outer surface of a tube is inherently different from condensation inside of a tube, it is expected that key interfacial behavior (*i.e.*, formation and motion of waves along the interface between liquid and vapor phases) will be similar between the two scenarios, and general trends regarding relative influence of body force and flow inertia will remain qualitatively the same across modules. To reiterate, although it is incorrect to expect similar heat transfer from the two modules, important aspects of hydrodynamic behavior

within CM-HT may be correctly assessed by analyzing images from CM-FV.

Fig. 1(b) shows the i.d. of the inner stainless-steel tube in CM-FV is 5.23 mm, the tube wall thickness is 0.41 mm, and the outer channel width is 12.2 mm. These dimensions were selected to provide a hydraulic diameter in the outer annulus similar to the 7.12-mm i.d. in CM-HT. Upstream adiabatic development lengths are provided for both FC-72 and water streams, with inlet and exit temperature and pressure measurements made within these regions using type-T thermocouples and STS absolute pressure transducers, respectively.

High-speed flow visualization images are captured at three locations along the tube length: the first spanning the first 55.9 mm of the condensation length, the second centered at the midpoint of the 587.88-mm condensation length, and the third covering the last 55.9 mm of the condensation length. Images are captured at two speeds (depending on flow rate of condensate): 2000 frames per second (fps) with pixel resolution of 2040×174, and 4000 fps with pixel resolution of 2040×81.

Temperature measurements are also made at 5 axial locations along the condensation length (this time inside of the inner stainless-steel tube), corresponding to the upstream and downstream edges of the first and last imaging windows, as well as the center of the channel (center of the middle imaging location). Each axial location consists of three type-T thermocouples, with two brazed 180° apart to the inner wall of the stainless-steel tube, and the third inserted directly into the water flow within the tube.

2.3. Experimental facility

The facility used for the current tests was developed as part of NASA's ongoing FBCE and used as a brass-board system for testing flight hardware prototypes and troubleshooting experiment operations. Fig. 1(c) and (d) provide a schematic and photo of the facility, respectively, with the photo in Fig. 1(d) showing the facility configured for testing in vertical upflow orientation.

The schematic in Fig. 1(c) shows the working fluid FC-72 is circulated by a Micropump gear pump. Flow passes through a 5-μm filter to remove entrained particulates prior to entering a Coriolis flow meter. Flow then enters the bulk heater, used to provide the desired thermodynamic state at the module inlet for each test case.

The bulk heater used in the current experiments is configured to reflect the manner in which it will be utilized in the final ISS experiments. Two modes of operation are used, one with PID control of heater metal temperature and one with constant power provided to the bulk heater. Test matrix cases which call for superheated inlet conditions are run using PID temperature control, and those which require a saturated mixture at the module inlet use constant power.

After exiting the bulk heater, the working fluid passes through a short insulated length and enters the test section. As outlined in the preceding subsections, flow through each module is condensed by counterflow of cooling water provided by a water conditioning unit. This unit consists of a Merlin M33 chiller, pump, filter, and digital flow controllers for setting flow rate (which is measured using Coriolis flow meters, similar to FC-72 flow).

Exiting the test section, flow passes through a secondary condenser used to ensure the test fluid is returned to a subcooled liquid state prior to returning to the pump. Water flow for the condenser is also provided by the water conditioning unit, with water flow rate through the secondary condenser controlled independently from that for the module.

Finally, the fluid passes the accumulator (used to account for fluid volume changes within the flow loop as well as adjust loop pressure through air-side pressure adjustment) and returns to the pump.

As indicated in Fig. 1(d), all fluid hardware other than the water conditioning unit are mounted on a rotating bench-top. This allows for quick transition between tests in vertical upflow, vertical downflow, and horizontal flow orientations.

2.4. Operating conditions, operating procedure, and measurement uncertainty

Operating conditions investigated in the current set of experiments reflect a subset of those planned for the ISS. Table 1 outlines target operating conditions for the current experiments, where every combination of FC-72 mass flowrate, water mass flowrate, operating pressure, and inlet quality is tested in vertical upflow, vertical downflow, and horizontal flow orientations.

Overall, tests across all three orientations include 29 cases in vertical upflow, 29 cases in vertical downflow, and 34 cases in horizontal flow, with experimental operating conditions spanning FC-72 mass velocities of G_{FC} = 50.3–360.3 kg/m^2 s, test section water cooling mass velocities *of* G_{H2O} = 129.2–388.4 kg/m^2 s, FC-72 test section inlet pressure of P_{in} = 127.0–132.1 kPa, bulk heater power of Pwr_{BH} = 304.2–1578.1 W, test section inlet thermodynamic equilibrium qualities of $x_{e,in}$ = 0.13–1.15, and test section exit qualities of $x_{e,out}$ = −0.50 to 0.47. Table 1 indicates 30 tests should be conducted, but this number was slightly adjusted for each orientation during experiment conduction.

It should be noted here that inlet and exit thermodynamic equilibrium qualities greater than 1.0 and less than 0 refer to superheated and subcooled conditions, respectively. They are calculated according to the expressions

$$x_{e,in} = \frac{Pwr_{BH} - \dot{m}_{FC} c_{p,f,FC} \left(T_{FC,sat} - T_{BH,in}\right)}{\dot{m}_{FC} h_{fg,FC}}, \tag{1}$$

and

$$x_{e,out} = \frac{Pwr_{BH} - \dot{m}_{FC} c_{p,f,FC} \left(T_{FC,sat} - T_{BH,in}\right) - \dot{m}_{\mathrm{H2O}} c_{p,f,\mathrm{H2O}} \left(T_{\mathrm{H2O},out} - T_{\mathrm{H2O},in}\right)}{\dot{m}_{FC} h_{fg,FC}}, \tag{2}$$

where Pwr_{BH}, $\dot{m}$, c_p, and h_{fg} are, respectively, the power supplied to FC-72 by the bulk heater, fluid mass flow rate, liquid specific heat, and enthalpy of vaporization. All fluid properties for each phase are evaluated at local pressures. It should also be noted that cases with superheated inlet conditions have inlet quality evaluated directly from measured temperature and pressure. Eq. (1) is only used for cases with saturated mixture inlet conditions and is evaluated after adjusting power supplied by the bulk heater, Pwr_{BH}, to account for heat loss.

Test cases were run by first setting FC-72 flow rate, water flow rate, and bulk heater power to levels necessary to achieve the desired inlet conditions. As the system approached steady state, tweaks were made to each of these parameters as well as to accumulator gas-side pressure (used to adjust module inlet pressure to

Table 1
Target operating conditions for current study.

G_{FC} [kg/m^2 s]	G_{H2O} [kg/m^2 s]	$P_{FC,in}$ [kPa]	$x_{e,in}$
50	130, 260, 390	130	1.0
100	130, 260, 390	130	1.0
100	390	130	0.4, 0.6, 0.8
150	130, 260, 390	130	1.0
200	130, 260, 390	130	1.0
200	390	130	0.4, 0.6, 0.8
250	130, 260, 390	130	1.0
300	130, 260, 390	130	1.0
300	390	130	0.4, 0.6, 0.8
350	390	130	0.4, 0.6, 0.8

the desired value) until all flow parameters match those desired for the test point. The system was then allowed to sit for 3–5 minutes to ensure no appreciable deviations from the steady-state operating conditions occurred.

After achieving the desired steady-state operating conditions for the test point, steady-state data was acquired for 2 min at a sampling rate of 200 Hz, then for three minutes at a sampling rate of 5 Hz. Sampling rate was controlled through LabView, and the rationale for use of two separate frequencies was to facilitate capture of dynamic phenomenon using a high sampling rate (as was done in a series of recent articles by the present authors [73,80–83]), while also capturing data at a lower sampling rate matching that to be used on the final ISS experiment. All data presented within the current study corresponds to the lower 5-Hz sampling frequency, and operating conditions reported in this study correspond to averages taken over the three minute, 5 Hz steady-state data acquisition period.

Data collection for all temperature, pressure, flow rate, and power measurements is handled by a cDaQ-9178 data acquisition system with one NI-9205 analog input module and four NI-9214 thermocouple modules, all controlled by LabView. Temperature measurements made with type-T thermocouples have uncertainty of ±0.4 °C, pressure measurements made with STS absolute pressure transducers have uncertainty of ±0.1%, flow rate measurements (and thus mass velocities) made with Coriolis flow meters have uncertainty of ±0.2%, and bulk heater power input calculated from voltage and current data has uncertainty of ±0.2 W. All properties are evaluated at local pressure using data obtained from NIST.

3. Condensate liquid distribution

As mentioned in the introduction, condensation flow regimes describe distribution of liquid and vapor phases within the condensation length, with transition criteria and associated regime maps available in the literature providing guidelines for what distribution may be expected for different ranges of operating conditions. Prior to analyzing the specifics of liquid film distribution for commonly defined flow regimes (*i.e.,* circumferentially uniform *annular* flow or liquid pooling near the bottom in *stratified* flow), it is useful to first discuss qualitative changes in flow behavior in response to competing influences of body force and flow inertia in different orientations. Flow visualization images for vertical downflow orientation will be omitted here, as downflow commonly exhibits annular co-current flow for all operating conditions and representative images may be found in other works [34].

3.1. Flow visualization image sequences

Fig. 2 provides image sequences of vertical upflow condensation corresponding to three different mass velocities, with all sequential images separated by 0.0125 s. Imaging in vertical upflow orientation was not performed using CM-FV (described in Section 2) due to time constraints on testing, so image sequences in Fig. 2 are adapted from the work of Park and Mudawar [35]. They investigated flow condensation of FC-72 in a smooth circular tube of comparable hydraulic diameter and condensation length to the present modules. Their original experimental work should be consulted for additional details.

Fig. 2(a) depicts images captured in the inlet region of the channel corresponding to G_{FC} = 13.32 kg/m^2 s and G_{H2O} = 6.09 kg/m^2 s. These operating conditions lead to *falling film* behavior observed within the channel, characterized by liquid motion counter to that of bulk vapor flow at the outset of the image sequence. Beginning with the sixth image, however, signs of a large liquid front passing through the channel in the same direction as vapor flow become apparent, likely acting to enforce conservation of mass within the channel in a time-averaged fashion. This is very similar to phenomenon investigated and modeled by the present authors in recent studies for vertical upflow boiling [82,83].

Fig. 2(b) shows similar results again captured in the inlet region of the channel, this time corresponding to moderate mass velocities of G_{FC} = 53.29 kg/m^2 s and G_{H2O} = 73.36 kg/m^2 s. The increase in FC-72 mass velocity leads to minimal liquid film motion, with the near-stationary liquid film advected slowly upwards by the fast-moving vapor core (commonly referred to as *flooding*). This leads to the formation of higher frequency, lower amplitude interfacial waves than were present in Fig. 2(a).

Finally, Fig. 2(c) provides images captured in the outlet region of the channel for mass velocities G_{FC} = 106.45 kg/m^2 s and G_{H2O} = 97.79 kg/m^2 s and shows how high condensate mass velocities lead to co-current flow of liquid and vapor phases (*climbing film* flow regime). This regime shows clear signs of larger amplitude interfacial waves as compared to Fig. 2(b), but without the periodicity present in Fig. 2(a).

Across all subfigures present in Fig. 2, it may be seen that increased mass velocity has a stabilizing effect on vertical upflow condensation, with increases transitioning liquid film motion from *falling film* to *flooding* to *climbing film* regimes. It is also important to note here that, across all condensate mass velocities, liquid film distribution is seen to be largely symmetric about the channel centerline.

Fig. 3 provides flow visualization image sequences captured at the middle of the channel in horizontal flow orientation, with individual images separated by 0.01 s. Fig. 3(a) corresponds to mass velocities of G_{FC} = 17.9 kg/m^2 s and G_{H2O} = 462.8 kg/m^2 s. Although faint, a clear liquid vapor interface is present near the centerline of each image. This is a key difference between internal (CM-HT) and external (CM-FV, shown here) flow condensation: internal flow condensation in horizontal orientation at low mass velocities is expected to exhibit signs of stratified flow, while external flow at low mass velocities can potentially lead to the module partially filling with liquid (depending on the position of inlet and outlet ports). Although manifesting differently, both conditions reflect the stratified nature of horizontal flow at low mass velocities.

Fig. 3(b) shows that, for higher mass velocities of G_{FC} = 67.3 kg/m^2 s and G_{H2O} = 462.0 kg/m^2 s, flow exhibits a more typical stratified pattern with some liquid present on the inner stainless-steel tube (condensation surface) but most liquid dripping off and moving along the bottom, adiabatic wall of the channel. This reflects expected internal flow behavior, where liquid film accumulates in the bottom of the channel, while the top surface remains exposed to vapor which is condensed and moves to the bottom of the channel due to body force.

Fig. 3(c) clearly illustrates how increased mass velocities of G_{FC} = 99.6 kg/m^2 s and G_{H2O} = 462.1 kg/m^2 s lead to a more nearly annular flow regime. Liquid content along the bottom (adiabatic) surface of the channel is reduced from Fig. 3(b), and significantly reduced from that seen in Fig. 3(a).

3.2. Summary of qualitative trends for condensate liquid behavior

In all flow visualization image sequences presented in the preceding subsection, the dominant competing effects were seen to be those of flow inertia (related to liquid flowrate) and body force (differing based on channel orientation). Fig. 4 presents schematics summarizing the effects competing influences of body force and flow inertia have on liquid distribution within the condensation length.

Fig. 4(a) provides a schematic for vertical upflow condensation. The left-hand figure shows how, at any given axial location along

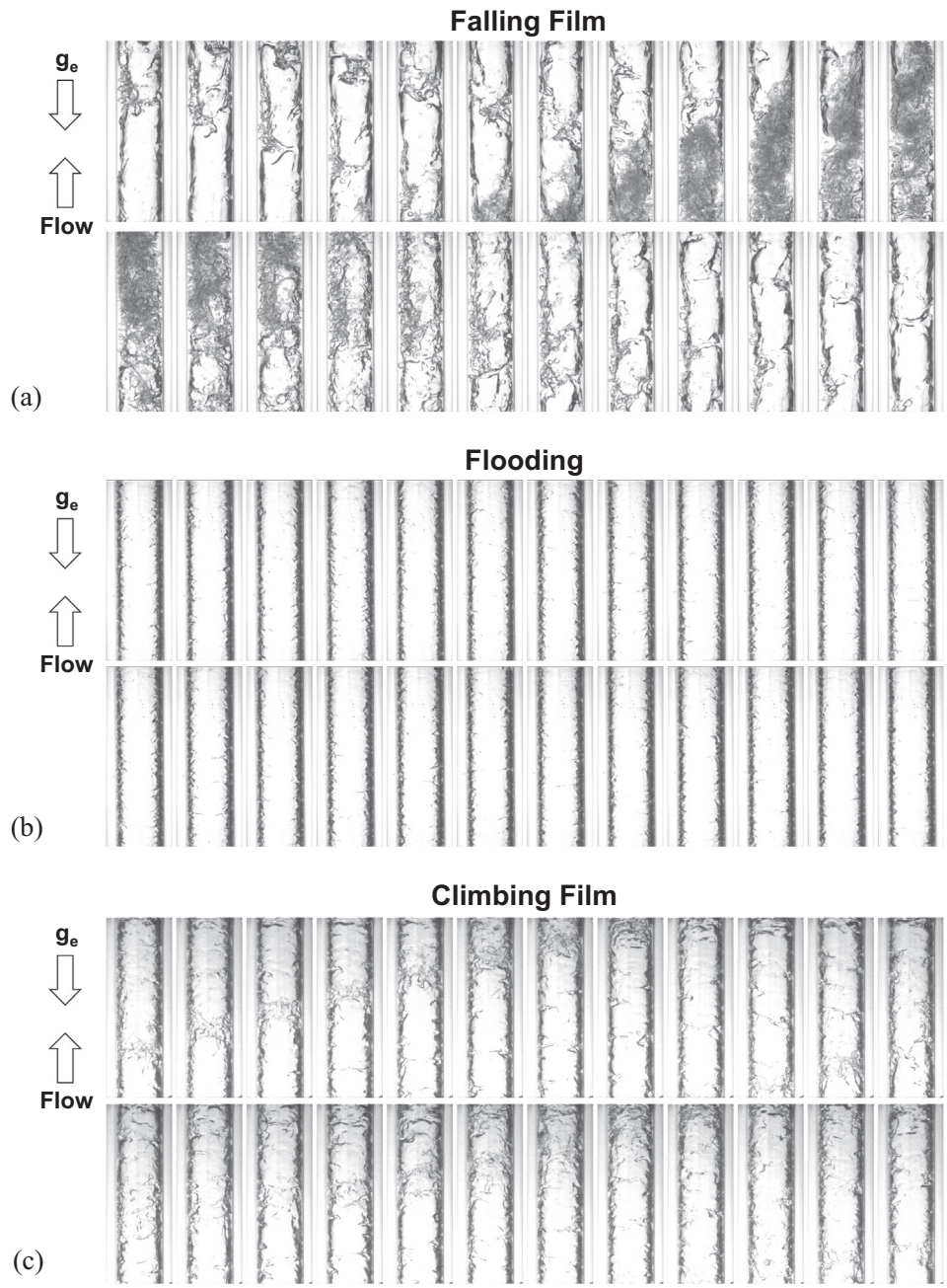

Fig. 2. Sequential images of (a) falling film in inlet region (centered at $z = 190$ mm) with $G_{FC} = 13.32$ kg/m^2 s and $G_{H2O} = 6.09$ kg/m^2 s, (b) flooding in inlet region with $G_{FC} = 53.29$ kg/m^2 s and $G_{H2O} = 73.36$ kg/m^2 s, and (c) climbing film in outer region (centered at $z = 952$ mm) with $G_{FC} = 106.45$ kg/m^2 s and $G_{H2O} = 97.79$ kg/m^2 s, with individual images in each sequence separated by 0.0125 s. Adapted from [35].

the condensation length, liquid film distribution is expected to be circumferentially symmetric. This is due to body force acting directly opposite to fluid motion, meaning while it affects liquid motion as it travels through the channel, it does not bias liquid to any particular location along the tube circumference.

The schematics in Fig. 4(a) illustrating axial flow characteristics (to the right of the axial cut discussed in the previous paragraph) illustrate how body force impacts transport behavior within the channel. At high mass flows, interfacial shear provided by the fast-moving vapor core is sufficient to advect liquid along the channel, and annular co-current flow (*climbing film*) is established. At low mass velocities, however, film motion may stagnate or even move counter to the direction of vapor flow, meaning periodic effects such as film breakup and droplet entrainment become important for liquid transport through the condensation channel. Flow regimes encountered for low mass velocities include *flooding*, *oscillating film*, and *falling film*.

Fig. 4(b) provides similar schematics for vertical downflow condensation. Similar to Fig. 4(a), the circumferential distribution of liquid is seen to be axisymmetric due to body force acting parallel to flow direction. Dissimilar from Fig. 4(a), however, is the fact that no appreciable differences in film motion are seen for low versus high mass flowrates. By acting in the same direction as fluid motion, body force has a stabilizing effect on liquid film motion, ensuring *annular co-current* flow for all operating conditions.

Fig. 3. Sequential images of horizontal flow captured at the middle of the channel (z = 294 mm) with (a) G_{FC} = 17.9 kg/m^2 s, G_{H2O} = 462.8 kg/m^2 s, $P_{FC,in}$ = 124.0 kPa, Pwr_{BH} = *315.3,* and $x_{e,in}$ = 1.06, (b) G_{FC} = 67.3 kg/m^2 s, G_{H2O} = 462.0 kg/m^2 s, $P_{FC,in}$ = 125.5 kPa, Pwr_{BH} = *1108.8,* and $x_{e,in}$ = 1.12, and (c) G_{FC} = 99.6 kg/m^2 s, G_{H2O} = 462.1 kg/m^2 s, $P_{FC,in}$ = 125.2 kPa, Pwr_{BH} = *1575.2,* and $x_{e,in}$ = 1.12, with individual images in each sequence separated by 0.01 s.

Fig. 4(c) uses an additional schematic for circumferential distribution to highlight how flow rate affects liquid distribution in horizontal flow condensation. For high mass flows, liquid film spreads evenly around the channel circumference, leading to *annular co-current* flow similar to that seen in vertical downflow orientation. At low mass flowrates body force drives liquid film to accumulate in the bottom of the channel, leading to flow regimes including *stratified*, *stratified wavy*, and *plug* flow regimes.

3.3. Utility of new method for flow regime identification

Information discussed in the preceding two subsections represents common knowledge for flow regimes in condensing flows, reaffirmed by numerous researchers over many decades of image analysis and modeling work. There is no disputing the role of flow regime on condensation heat transfer, and a number of researchers have proposed methods for predicting condensation heat transfer which depend on knowing/predicting flow regime within the condensation length [84–87].

Practically, this has translated to a need for system designers to validate two separate classes of design tools: one for determining condensation flow regime and one for determining condensation heat transfer coefficient (pressure drop applies here as well). The difficulty stems from the lack of visual access to liquid flow in condensing systems, necessitating construction of a second test section (as done in the current work) or complicated additions to standard condensation heat exchangers (often affecting heat transfer) to allow image capture. To overcome this limitation, the present work aims to present a new method for determining liquid film distribution and motion in condensing systems based entirely on temperature and pressure measurements.

4. Flow regime identification

Work on flow regime identification using temperature and pressure measurements was split into two areas of focus. The first is to determine whether liquid and vapor motion in vertical orientations is co-current (commonly *co-current annular* flow or *climbing*

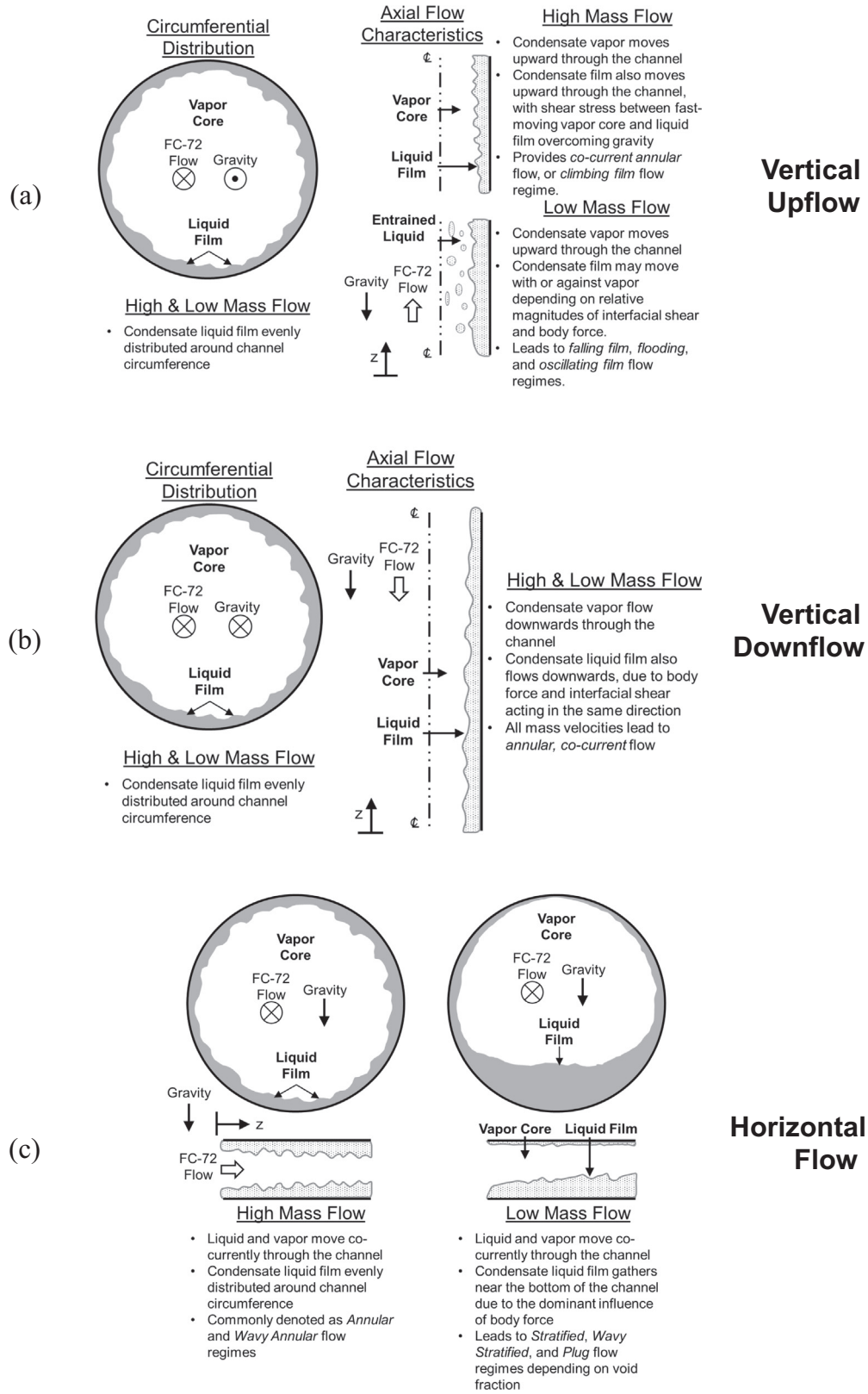

Fig. 4. Schematics of liquid film circumferential distribution and axial flow characteristics for (a) vertical upflow, (b) vertical downflow, and (c) horizontal flow orientations.

film flow regime) or counter-current (leading to *flooding, oscillating film*, and *falling film* regimes). The second involves detection whether flow in horizontal orientations is stratified (*stratified flow*, *wavy-stratified flow*, *plug flow*) or axisymmetric (*annular flow*, *slug flow*).

4.1. Co-current and counter-current flows

Conservation of mass is an important concept to keep in mind when attempting to determine whether vertical flow is co-current or counter-current. As discussed in conjunction with Fig. 2, low mass velocity cases in vertical upflow orientation lead liquid film to move counter to vapor motion or remain largely static. In both cases some other mechanism is needed to remove accumulating liquid phase from the condensation length, otherwise the channel would become filled entirely with liquid and condensation would no longer take place. This mechanism may be glimpsed in Fig. 2(a), which shows falling film giving way to the passage of a large liquid front, likely formed by falling film liquid accumulating in the entrance of the channel then departing. This ensures mass flow into the channel balances with that out of the channel in a time-averaged fashion.

Although less noticeable than for *falling film*, other counter-current regimes such as *oscillating film* and *flooding* also rely on periodic transport of liquid phase out of the condensation length to ensure mass conservation. As mass velocity is increased and flow within the channel exhibits *climbing film* behavior, this periodic mechanism is no longer necessary as both liquid and vapor move along the channel together.

As discussed at great length in prior works dealing with boiling in a vertical channel, this periodic motion of liquid through the channel is observable in both pressure and temperature measurements [80–83]. Based on this, plots of temperature and pressure versus time for different operating conditions in vertical upflow and vertical downflow (used for comparison purposes, as downflow condensation is expected to always be co-current and annular) were used as a starting point for analysis.

Fig. 5(a)–(d) provide plots of temperature and pressure versus time, captured over the last 100 s of each respective steady-state data acquisition period. Temperature measurements displayed correspond to the first, third, fifth, seventh, ninth, and eleventh axial measurement stations within CM-HT (see the schematic in Fig. 1(a) for details on exact positions). Each curve represents an average of three circumferentially spaced thermocouple measurements on the tube wall at each axial location, as indicated by the schematic inset in Fig. 5(a).

Fig. 5(a) and (b) correspond to vertical upflow with superheated vapor inlet conditions with $G_{FC} = 303.3$ kg/m^2 s and $G_{FC} = 63.1$ kg/m^2 s, respectively. Immediately apparent is the significant difference in pressure oscillatory behavior between the high and low flowrate cases. Fig. 5(a) illustrates minimal pressure fluctuations are present for high mass velocities (where *co-current annular* flow is expected), while Fig. 5(b) showcases pressure changes on the order of 20 kPa (for conditions where *falling film* flow is expected).

Comparison of temperature fluctuations for the two sets of operating conditions shown in Fig. 5(a) and (b) yields fewer concrete conclusions than for inlet and exit pressures, with no clear differences in amplitude of fluctuations. It is worth noting that stainless steel wall temperature values are decreased for the case with low FC-72 mass velocity, a fact which will become important in subsequent figures.

Fig. 5(c) and (d) show similar plots corresponding to vertical downflow condensation with mass velocities of $G_{FC} = 301.9$ kg/m^2 s and $G_{FC} = 53.8$ kg/m^2 s, respectively. Amplitudes of pressure fluctuations for both cases are significantly smaller than those observed in Fig. 5(b), with Fig. 5(d) in particular exhibiting minimal pressure fluctuations. This is attributable to the low FC-72 flow rate in Fig. 5(d) allowing gravity to dominate flow behavior. Comparison of temperature fluctuations across Fig. 5(c) and (d) again reveal no clear trends.

Continuing the present analysis to fully determine conditions for which vertical flows exhibit counter-current and co-current regimes, Fig. 6 presents *scaled temperature and pressure fluctuations*. These are calculated according to the relationships

$$\text{scaled temperature fluctuation} = \frac{T'}{T_{ave}} \times 100\% = \frac{0.5(\max(T_{0-n}) - \min(T_{0-n}))}{mean(T_{o-n})} \times 100\%, \quad (3)$$

and

$$\text{scaled pressure fluctuation} = \frac{P'}{P_{ave}} \times 100\% = \frac{0.5(\max(P_{0-n}) - \min(P_{0-n}))}{mean(P_{o-n})} \times 100\%, \quad (4)$$

where T_{0-n} represents instantaneous temperature measurements in degrees Celsius spanning time t_0 to t_n., and P may refer to inlet or exit pressure (in kPa) depending on the subscript used.

Fig. 6(a) provides plots of scaled temperature fluctuations averaged along the channel length versus mass velocity for cases with superheated inlet conditions in both vertical upflow (top plot) and vertical downflow (bottom plot). It should be noted here that channel length averaged values are calculated by using area-weighted averaging of all eleven local values for each set of operating conditions, and that vertical lines depicting boundaries between counter-current flow, co-current flow, and the transition between are intended only to apply to vertical upflow results: vertical downflow exhibits *co-current annular* flow for all operating conditions shown here.

A clear convergence in values of scaled temperature fluctuations is seen for vertical upflow in Fig. 6(a) as mass velocity is increased, with mass velocities in the range $G_{FC} > 125$ kg/m^2 s exhibiting no appreciable changes as mass velocity is changed, while those below $G_{FC} = 125$ kg/m^2 s increase significantly. Vertical downflow results in the bottom plot yield no clear trends, with $G_{FC} \sim 100$ kg/m^2 s cases deviating from others for unclear reasons.

Similar plots of channel length average scaled temperature fluctuations for cases with saturated mixture inlet conditions are shown in Fig. 6(b). The top plot (again corresponding to vertical upflow) presents a convergence in values for high mass velocity cases as was seen for upflow in Fig. 6(a), only this time values do not converge until somewhere between $G_{FC} = 200$–300 kg/m^2 s. This is likely attributable to increased liquid content present in the channel for cases with saturated inlet conditions requiring higher flowrates to move out of counter-current flow regimes and into *co-current annular* flow.

Vertical downflow results in Fig. 6(b) depict two clear modes of oscillatory behavior exist for cases with saturated mixture inlet conditions. At the lowest mass velocity of $G_{FC} \sim 100$ kg/m^2 s scaled temperature fluctuations are at a maximum amplitude of ~3.5%, but for the higher flowrate of $G_{FC} \sim 200$ kg/m^2 s values drop from ~3.5% to 1% as inlet quality increases from $x_{e,in} \sim 0.4$ to $x_{e,in} \sim 0.8$. Higher values of mass flowrate all show scaled temperature fluctuations of ~1%, which is in line with 'converged' values in the other three plots from Fig. 6(a) and (b). It is believed this large difference between low and high flowrate cases is attributable to the presence of large interfacial waves on the liquid film, something discussed extensively for a variety of falling film and gravity driven flow configurations [88–94].

Fig. 6(c) shows scaled pressure fluctuations for both vertical upflow and vertical downflow orientations with superheated vapor

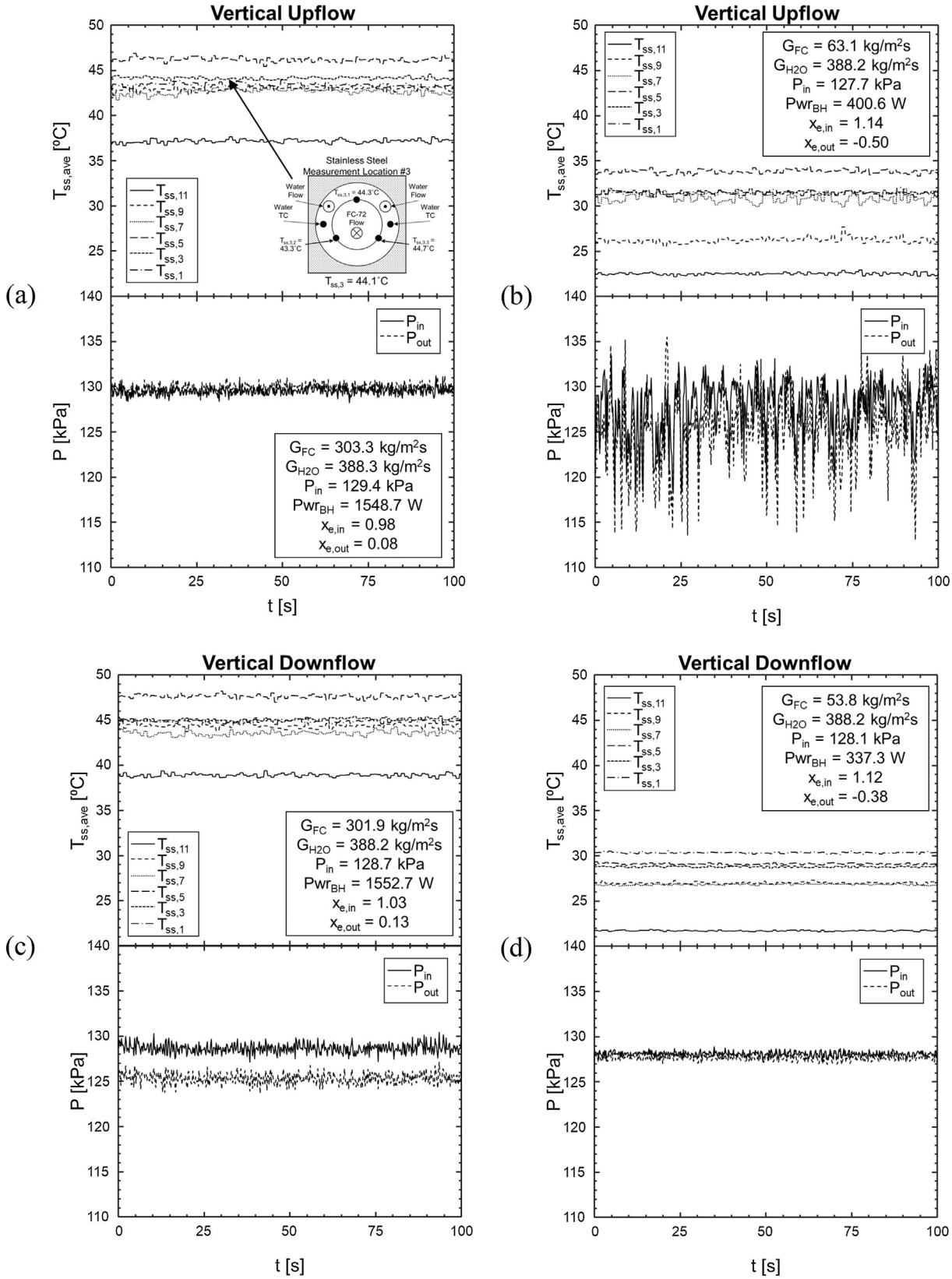

Fig. 5. Plots of stainless steel wall temperature and CM-HT inlet and outlet pressures for (a) vertical upflow with $G \sim 300$ kg/m^2 s, (b) vertical upflow with $G \sim 60$ kg/m^2 s, (c) vertical downflow with $G \sim 300$ kg/m^2 s, and (d) vertical downflow with $G \sim 50$ kg/m^2 s.

inlet conditions, with the top plot corresponding to inlet pressure data and the bottom plot to exit pressure. These provide the strongest evidence of a transition between counter-current and co-current regimes, with scaled pressure fluctuations 4–5 times higher for low flowrates (6–8%) in vertical upflow orientation than high flowrates (1–2%), indicating counter-current regimes are

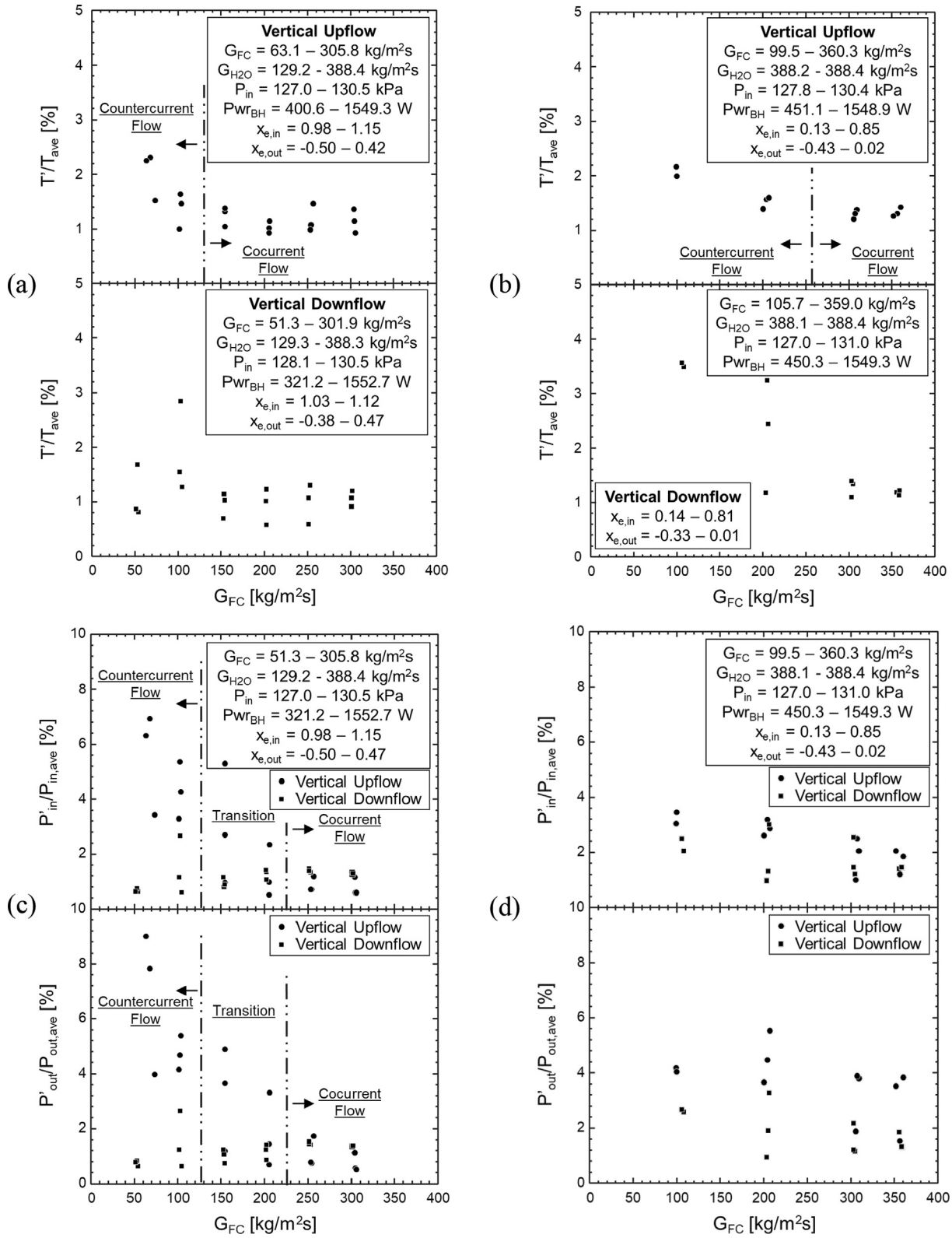

Fig. 6. Plots of scaled temperature fluctuations versus mass velocity for (a) superheated vapor and (b) twophase mixture inlet conditions, and scaled pressure fluctuations at channel inlet and outlet for (c) superheated vapor and (d) two-phase mixture inlet conditions.

present for lower mass velocities. Scaled pressure fluctuations in vertical downflow orientation stay within the 1–2% range for all flowrates tested, and vertical upflow results are seen to converge to identical values for flowrates above $G_{FC} \sim 225$ kg/m^2 s, strongly suggesting *co-current annular* flow (*climbing film* in upflow) is present for both orientations. At moderate mass velocities in the range $G_{FC} \sim 100$–200 kg/m^2 s flow appears to be transitioning from counter-current to co-current (evidenced by scaled pressure

fluctuations) leading these cases to be labeled 'transition' in Fig. 6(c). The fact scaled pressure fluctuations for these operating conditions have not yet converged to the 1–2% range seen for vertical downflow means some oscillatory behavior is likely still present, but likely only in the form of *flooding* flow regime as opposed to the *falling film* flow regime seen for the lowest mass velocity cases.

Finally, Fig. 6(d) provides plots of scaled pressure fluctuations versus mass velocity for both vertical upflow and downflow cases with saturated mixture inlet conditions. Values for the two orientations are seen to converge as mass velocity is increased, but without the clear demarcations visible as for cases with superheated vapor inlet seen in Fig. 6(c).

In summary for the present subsection, analysis of transient temperature and pressure results revealed the clear presence of significant oscillatory behavior in vertical upflow for mass velocities $G_{FC} < 125$ kg/m^2 s due to counter-current flow behavior (*falling film* flow regime). For mass velocities $G_{FC} > 225$ kg/m^2 s both temperature and pressure results reveal scaled fluctuations converge between vertical upflow and downflow orientations, leading to the conclusion *co-current annular* flow is present for these operating conditions (*climbing film* flow regime in upflow). Mass velocities in the range $G_{FC} \sim 125$–225 kg/m^2 s were labeled as transitional due to a lack of significant oscillatory behavior in vertical upflow, but still enough to prevent convergence with vertical downflow data. These points are likely experiencing some combination of *oscillating film* and *flooding* flow regimes.

It should also be noted it is possible amplitude of scaled fluctuating parameters may be similar for low flowrate cases (experiencing counter-current flow) and very high flowrate cases (experiencing dynamic film behavior). Detection of flow regime is still possible by determining whether an increase in flowrate leads to a decrease in oscillatory behavior (indicating flow is counter-current, approaching co-current) or an increase in oscillatory behavior (indicating flow is already co-current). The reverse will also be true if a small decrease in flowrate is used as a test.

4.2. Stratified and axisymmetric horizontal flows

Having presented a method for distinguishing between co-current and counter-current vertical flows, as well as the significant influence of interfacial waves on heat transfer in gravity-dominated downward flows, we finally discuss the detection of stratified and axisymmetric flows in horizontal orientation. Recalling trends discussed when analyzing Fig. 3, increases in mass velocity are seen to lead to a 'spreading' of liquid film around the channel circumference. At low mass velocities condensed liquid is expected to pool in the bottom of the condensation channel while hot vapor remains exposed to the top surface (leading to *stratified*, *wavy-stratified*, or *plug* flow regimes), behavior which should lead to clear gradients in circumferential temperature.

Towards this end Fig. 7 provides plots of local stainless-steel wall temperatures, T_{SS}, and water temperatures, T_{H2O}, averaged over the steady-state data acquisition period at all eleven axial measurement locations. Values of standard deviation σ_{SS} and σ_{H2O} for each respective set of local temperature measurements are also calculated and plotted versus position along the condensation length in the bottom subplots. These values are calculated according to the relationships

$$\sigma_{SS} = \sqrt{\frac{1}{N-1}\sum_{n=1}^{N}\left(T_{SS,n} - \bar{T}_{SS}\right)^2} \tag{5}$$

for stainless-steel temperatures, and

$$\sigma_{\mathrm{H2O}} = \sqrt{\frac{1}{N-1}\sum_{n=1}^{N}\left(T_{\mathrm{H2O},n} - \bar{T}_{\mathrm{H2O}}\right)^2} \tag{6}$$

for water. As described in Fig. 1(a), CM-HT contains three stainless-steel surface temperature measurements (spaced 120° apart) and two water temperature measurements (spaced 180° apart) at each axial location, meaning $N = 3$ for σ_{SS} and $N = 2$ for σ_{H2O}, and $\bar{T}$ is the average of these local values. The only exception to this is the first axial measurement station for stainless-steel wall temperatures where one of the three thermocouples has been omitted due to systematic errors resulting from instrumentation.

Fig. 7(a) provides plots of temperatures and standard deviations between associated measurements for vertical upflow, vertical downflow, and horizontal flow orientations, all with superheated vapor inlet conditions and $G_{FC} \sim 300$ kg/m^2 s. All three orientations show some local variations in values of standard deviation between circumferentially spaced temperature measurements, but no systematic bias, with all standard deviations falling within 0–3 °C.

Fig. 7(b) shows similar results for all three orientations again with $G_{FC} \sim 300$ kg/m^2 s, this time corresponding to inlet qualities of $x_{e,in} \sim 0.80$. Results again indicate little difference in deviation between circumferentially spaced measurements for different operating conditions.

This trend changes in Fig. 7(c), however, which provides temperature results for all three orientations with $G_{FC} \sim 100$ kg/m^2 s and superheated vapor inlet conditions. Vertical upflow and vertical downflow results in Fig. 7(c) again appear similar to one another, but horizontal flow results show significant deviation by one of the three thermocouples at all axial stations, with maximum values of standard deviation reached in the downstream region of the channel. This behavior is indicative of stratified flow conditions with two thermocouples at circumferential locations covered by subcooled liquid, while the third location remains exposed to hot vapor (with a thin intervening liquid film). The final measurement location shows all three temperature measurements collapsed back to a single value, and it can be inferred that complete condensation has been achieved by this point along the channel length (exit quality for the case is given as $x_{e,out} = -0.25$ indicating subcooled liquid conditions at the exit).

It is worth noting here that differences in water temperatures remain largely constant for both cases where no clear circumferential gradients are present (Fig. 7(a), (b), and the vertical orientations in (c)) as well as for horizontal flow in Fig. 7(c) where gradients are clearly visible for stainless-steel temperatures. This indicates water temperatures are insufficient to determine condensate liquid distribution (wall temperatures must be used); however, water temperatures are measured at the sides and not the top of the flow channel in the current tests, meaning it is possible different water measurement locations might show some signs of stratification.

Fig. 7(d) rounds out the picture by providing temperature information for all three orientations with $G_{FC} \sim 100$ kg/m^2 s and $x_{e,in} \sim 0.80$. Results again show no appreciable trends for vertical upflow and downflow orientations, while horizontal flow again shows a clear divergence of values in the up- and mid-stream regions indicating the presence of stratified flow.

Fig. 8 summarizes trends from Fig. 7 by plotting channel length averaged values of stainless-steel wall temperature standard deviations versus mass velocity for all cases in the dataset. Immediately apparent are the high standard deviation values for horizontal flow at low mass velocities, commonly 4–5 times higher in magnitude

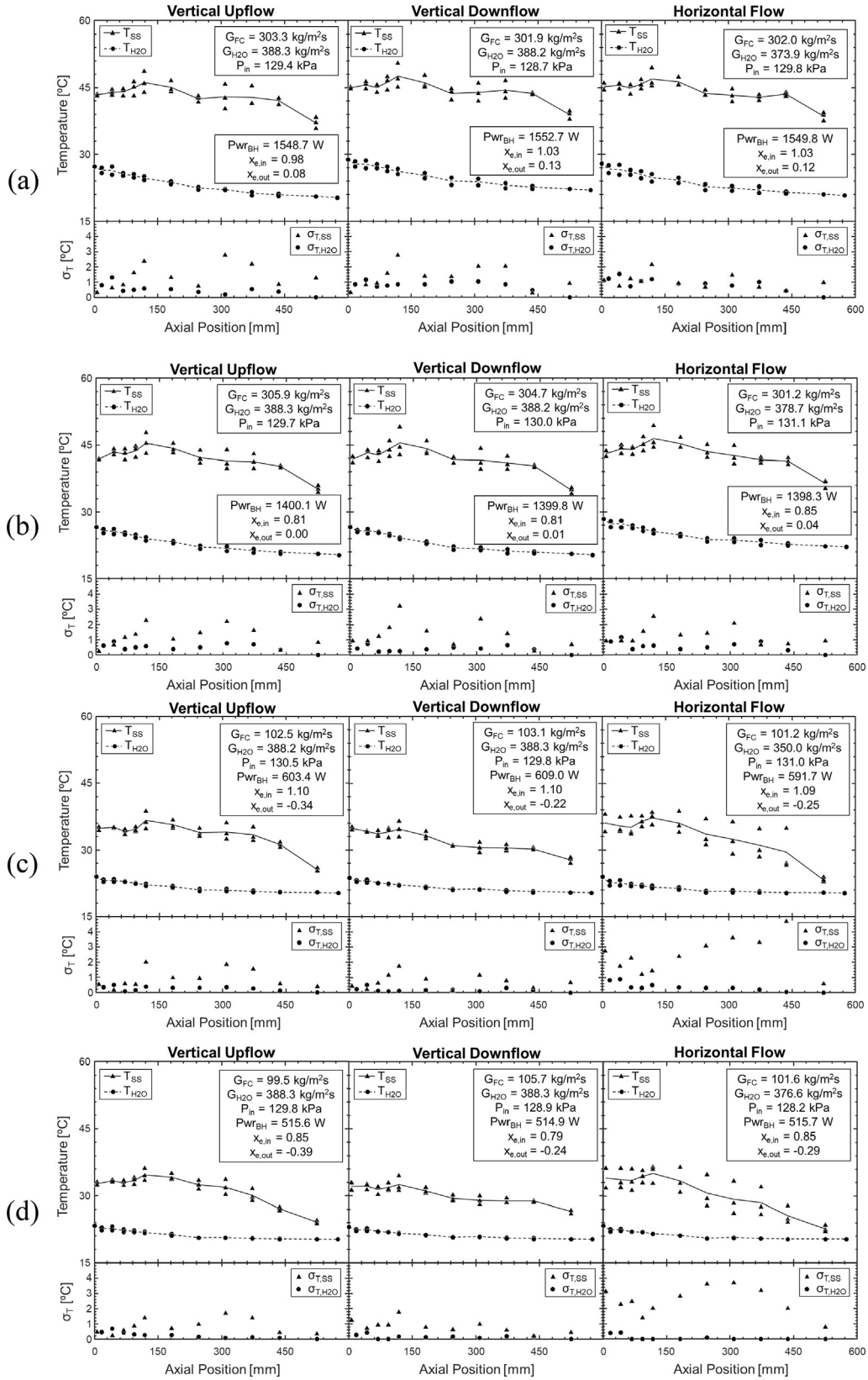

Fig. 7. Plots of stainless steel (T_{ss}) and water (T_{H2O}) temperature measurements at all axial locations as well as standard deviation between respective measurements in all three orientations for (a) $G_{FC} \sim 300$ kg/m^2 s and $x_{e,in} \sim 1.00$, (b) $G_{FC} \sim 300$ kg/m^2 s and $x_{e,in} \sim 0.80$, (c) $G_{FC} \sim 100$ kg/m^2 s and $x_{e,in} \sim 1.10$, and (d) $G_{FC} \sim 100$ kg/m^2 s and $x_{e,in} \sim 0.80$.

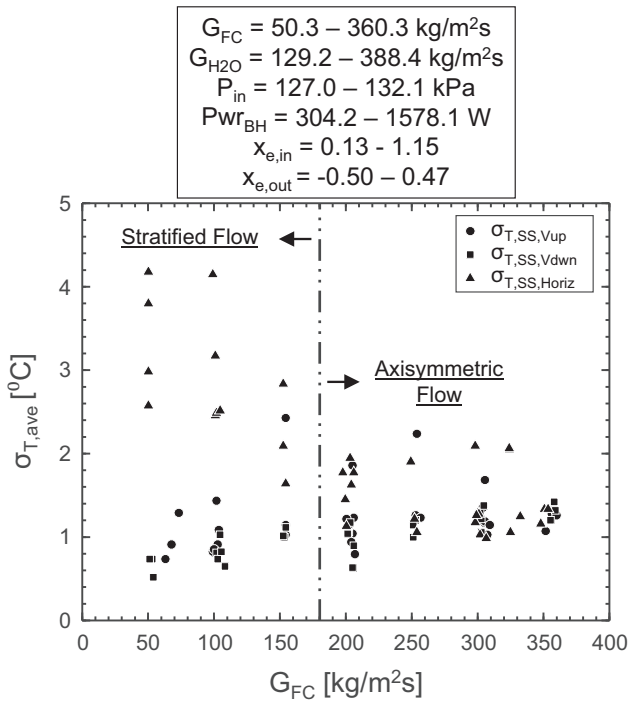

Fig. 8. Standard deviation between circumferential stainless-steel wall temperature measurements versus mass velocity for all three orientations. Values show signs of convergence by $G \sim 200$ kg/m^2 s, indicating this is the mass velocity at which horizontal flow transitions from *stratified* to *annular* flow in the current test section.

than their vertical upflow and downflow counterparts. As mass velocity increases, standard deviation values for horizontal flow are seen to decrease, approaching convergence with upflow and downflow near $G_{FC} \sim 200$ kg/m^2 s and exhibiting no noticeable differences from these orientations by $G_{FC} \sim 350$ kg/m^2 s. Based on this a clear transition point from stratified flows (*stratified*, *wavy-stratified*, and *plug* flow regimes) to axisymmetric flows (*annular*, *wavy-annular*, and *slug* flow regimes) is identified at $G_{FC} \sim 175$ kg/m^2 s and marked with a vertical dashed line. Similar to the note when discussing demarcations on Fig. 6, this line should only be taken to apply to horizontal flow cases (vertical upflow and downflow are seen to be axisymmetric for all operating conditions), and is meant to reflect the general transition from stratified to axisymmetric flow (which is a smooth process and not a step function).

4.3. Summary of new method for identifying condensation flow regime

The preceding subsections provide a new methodology for determining (1) whether flow in vertical orientations is co-current or counter-current and (2) whether flow in horizontal orientations is stratified or axisymmetric. Table 2 summarizes key points of the approach for each and provides guidelines for utilization in other experimental systems.

It is worth noting that all analysis in the present section assumes uniform flow of cooling water through the module annulus. Thermocouple insertion and routing paths through the annulus may lead to asymmetry depending on module design, and these effects should be considered when applying the present methodology to different test sections.

5. Comparison of results with flow regime maps

Having provided classification of flow regime observed using temperature and pressure measurements in the previous section, it is now useful to compare identified regimes with those predicted by transition criteria commonly used in literature. These are typically analytically formulated to capture key physics and empirically closed based on data used by respective authors. Comparison of results thus serves two purposes: (1) to validate that flow regimes identified using the new methodology are qualitatively in line with common predictions, and (2) to assess the ability of predictive tools to accurately capture the experimental flow regime trends presented in Section 4.

5.1. Vertical upflow condensation regime map

Flow regime maps for vertical upflow condensation are rarely found due to the undesirable role of body force destabilizing liquid film motion in this orientation leading designers to give preference to other orientations (primarily vertical downflow and horizontal flow). As mentioned in Section 1, however, significant work on modeling flow regime transitions in vertical upflow was done by Wallis [48]. He introduced a parameter C used for classifying flow regimes, defined as

$$C = \sqrt{j_g^*} + \sqrt{j_f^*}, \tag{7}$$

where j_g^* and j_f^* are dimensionless superficial velocities of vapor and liquid, respectively. These are in turn defined as

$$j_g^* = \frac{j_g}{\sqrt{gD_i\left(\rho_f - \rho_g\right)/\rho_g}} \tag{8}$$

and

$$j_f^* = \frac{j_f}{\sqrt{gD_i\left(\rho_f - \rho_g\right)/\rho_f}}, \tag{9}$$

where D_i is the diameter of the condensation tube and j_g and j_f are vapor and liquid superficial velocities, respectively, defined as

$$j_g = \frac{x_e G_{FC}}{\rho_g} \tag{10}$$

and

$$j_f = \frac{(1 - x_e)G_{FC}}{\rho_f}. \tag{11}$$

Specifying different values of C as representing different flow regimes allows transition criteria to be expressed in terms of relevant influences of body force, phase inertia, and phase mass fraction within the condensation length. These parameters have been shown throughout the study to be the dominant factors governing flow regime in vertical upflow condensation.

A recent study by Park and Mudawar [35] adapted Wallis' original methodology for use in predicting flow regime during vertical upflow condensation of FC-72 in a smooth tube with inner diameter $D_i = 11.89$ mm, comparable to the 7.12-mm value of the current test section. Due to this similarity their transition criteria are evaluated in the present study, given as $C = 0.85$ for the transition from *falling film* to *oscillating film*, $C = 1.0$ for *oscillating film* to *flooding*, and $C = 1.21$ for *flooding* to *climbing film*.

The flow regime map of Park and Mudawar [35] is shown in Fig. 9(a), with data from the current experiments evaluated using the transition criteria indicated (meaning symbols shown are predicted based on local operating conditions). It should be noted here that experimental values presented correspond to locally calculated quality values at all 11 axial measurement locations along the channel length and fluid properties evaluated at the channel inlet pressure. Locations with qualities $x_e > 0.99$ and $x_e < 0.01$ are

Table 2
Summary of flow regime identification approach in each orientation.

Orientation	Co-current vs. Counter-current Flow	Stratified vs. Axisymmetric Flow	General Notes
Vertical Upflow	• Calculate scaled temperature and pressure fluctuations • If values decrease for increased mass velocities, flow is counter-current (*falling film, oscillating film, flooding* flow regimes) • If values remain constant for changes in mass velocity, flow is co-current (*co-current annular, slug* flow regimes)	• Flow is axisymmetric for all operating conditions due to the role of body force acting opposite to flow (thus not creating any bias for circumferential film distribution)	• Ability to detect appreciable temperature and pressure fluctuations depends on thermal mass of condensation surface, magnitude of condensation length • May have difficulty applying co-current/counter-current test to data collected in short micro-channel heat sinks
Vertical Downflow	• Flow is co-current for all mass velocities due to role of body force aiding liquid film motion • Large values of scaled temperature fluctuations may be present for low mass velocities due to dominance of interfacial waves on film heat transfer	• Flow is axisymmetric for all operating conditions due to the role of body force acting parallel to flow direction	• Additional investigation on the transition between interfacial wave and vapor shear dominated heat transfer regimes necessary
Horizontal Flow	• Flow is co-current for all mass velocities	• Necessary to have multiple circumferentially spaced condensation surface temperature measurements (with at least 2 spaced 180° apart along the body force vector) • Calculate standard deviation between all circumferentially spaced temperature measurements • If values decrease as mass velocity is increased, flow is stratified (*stratified, wavy-stratified, plug* flow regimes) • If values remain neutral or increase slightly as mass velocity increases, flow is axisymmetric (*annular, wavy-annular, slug* flow regimes)	• Similar to the note for vertical upflow, ability to detect circumferential temperature gradients depends on thermal mass of condensation surface • May also be difficult to implement for micro-channel heat sinks
Inclined Channels (Extension)	• Depending on channel inclination and test section geometry it may be necessary to test if flow is co-current • Same approach as described for vertical upflow should be adopted	• Depending on channel inclination and test section geometry it may be necessary to test if flow is stratified • Same approach as described for horizontal flow should be adopted	• Testing of inclined channels necessary to determine utility of criteria as a function of orientation angle

assigned values of 0.99 and 0.01, respectively, to avoid dividing by zero in calculations. Full details on calculation of local quality values is outside the scope of the present work and may be found in the companion study [79].

Fig. 9(b) provides a plot of C versus FC-72 mass velocity for all vertical upflow cases. This plot is intended to highlight how predictions of flow regime change as mass velocity is increased, with low mass velocity cases predicted to exhibit mostly *falling film*, *oscillating film*, and *flooding* behavior, while higher mass velocity cases transition to predominantly climbing film flow regime.

Fig. 9(c) re-plots this information, now expressing only a channel average flow regime instead of the local values shown in Fig. 9 (a) and (b). Channel-length average flow regime is calculated by determining an area-weighted value of C for each test case (just as area weighted scaled fluctuating parameters and standard deviations were calculated in Sections 4.1 and 4.2) and evaluating the given transition criteria based on that average value.

Also shown in Fig. 9(c) are the transition boundaries originally created as a part of Fig. 6. These highlight the regimes as identified from experimental temperature and pressure data, allowing for easy comparison with those predicted by the map of Park and Mudawar.

Comparison of results is provided in Table 3 and indicate that the map of Park and Mudawar does a good job of capturing trends observed experimentally. At low mass velocities where counter-current flow is expected, their map predicts 4/8 cases to be *falling film* flow regime, and 7/8 cases to be something other than *climbing film* (*co-current annular* flow).

For moderate mass velocities where flow is expected to transition between counter-current and co-current flow, the map of Park and Mudawar predicts 1 *oscillating film*, 1 *flooding*, and 7 *climbing film* cases. This indicates their transition criteria are generally reflective of experimental results, with potentially a slightly early transition to climbing film flow regime compared to what is observed.

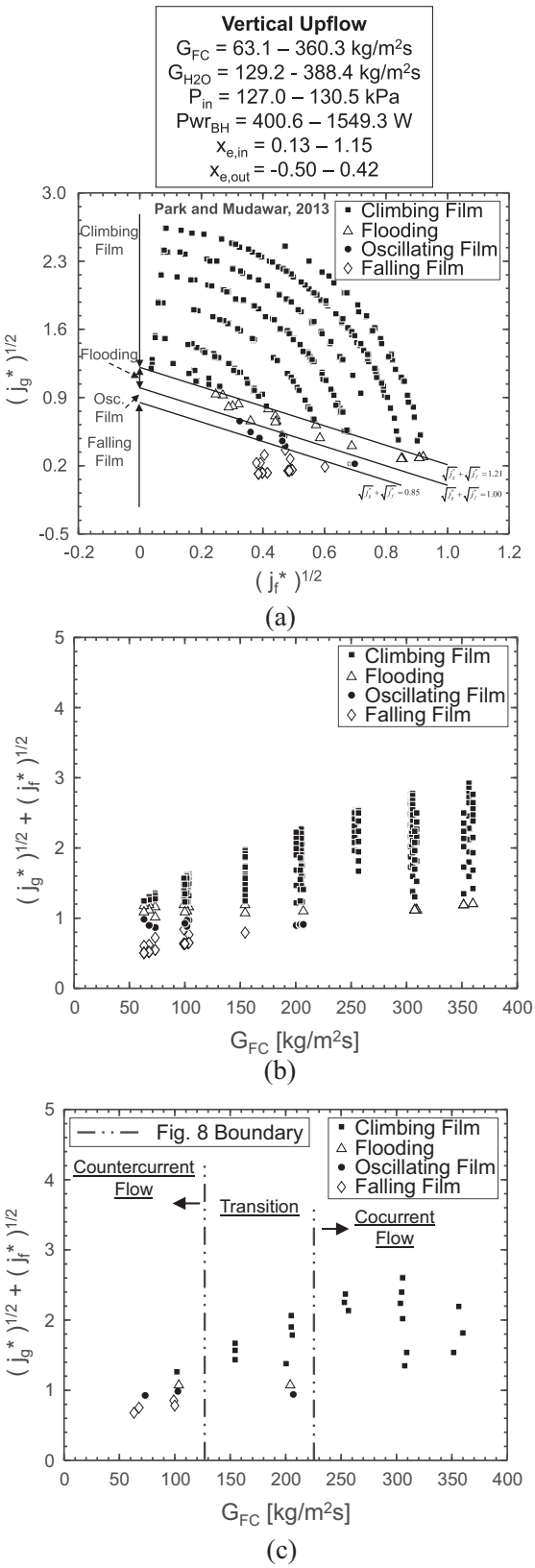

Fig. 9. (a) Vertical upflow condensation regime map of Park and Mudawar [35] providing predictions of flow regime for all local measurements in the current dataset, along with (b) predicted flow regime versus mass velocity and (c) channel length-average predicted flow regime versus mass velocity.

Finally, for high mass velocities their map correctly identifies all 12 experimentally identified co-current flow cases as *climbing film* flow regime.

5.2. Horizontal flow condensation regime maps

Compared to the limited options available for prediction of vertical upflow condensation flow regime, a prolific number of maps have been created for horizontal flow. Fig. 10 provides evaluation of four of the numerous available, selected due to their compatibility with the present experiment work and their presence in the overall condensation literature. Results for each map are also summarized in Table 4, similar to that done in Table 3 for Fig. 9.

Fig. 10(a) starts by presenting the map of Park et al. [36], created based on flow of FC-72 through a smooth circular tube. Their approach follows that originally outlined by Soliman [53,54] and expresses transition criteria in terms of modified Weber number We^* and the Lockhart-Martinelli parameter X_{tt}. These parameters are defined according to the relationships

$$We^* = 2.45Re_g^{0.64}\left(\frac{\mu_g^2}{\rho_g\sigma D}\right)^{0.3}/\phi_g^{0.4} \text{ for } Re_f \leqslant 1250, \tag{12a}$$

$$\text{and } We^* = 0.85Re_g^{0.79}\left(\frac{\mu_g^2}{\rho_g\sigma D}\right)^{0.3}\left[\left(\frac{\mu_g}{\mu_f}\right)^2\left(\frac{\rho_f}{\rho_g}\right)\right]^{0.084}\left(\frac{X_{tt}}{\phi_g^{2.55}}\right)^{0.157}$$

$$\text{for } Re_f > 1250, \tag{12b}$$

where

$$Re_g = x_e G_{FC} D/\mu_g, \tag{13}$$

$$Re_f = G_{FC}(1-x_e)D/\mu_f, \tag{14}$$

$$X_{tt} = \left(\frac{1-x_e}{x_e}\right)^{0.9}\left(\frac{\rho_g}{\rho_f}\right)^{0.5}\left(\frac{\mu_f}{\mu_g}\right)^{0.1}, \tag{15}$$

$$\text{and } \phi_g = 1 + 1.09X_{tt}^{0.039}. \tag{16}$$

Using these dimensionless groups originally presented by Soliman [53,54], Park et al. [36] defined their flow regime transition criteria as

$$\text{Stratified}: We^* < 6.03, \tag{17a}$$

$$\text{Stratified to wavy stratified}: 6.03 \leqslant We^* < 19.39, \tag{17b}$$

$$\text{Wavy stratified to wavy - annular with gravity influence}: 19.39 \leqslant We^* < 25.46, \tag{17c}$$

$$\text{Wavy - annular without gravity influence}: We^* \geqslant 25.46. \tag{17d}$$

Table 3
Summary of flow regime identification approach in vertical upflow.

Experimentally identified flow regime	Number of experimentally determined cases	Predictions by Park and Mudawar [35]	Percent correct
Counter-current Flow (*falling film* flow regimes)	8	4 falling film, 2 oscillating film, 1 flooding, 1 climbing film	50% (87.5%)
Transition (*oscillating film*, *flooding* flow regimes)	9	1 oscillating film, 1 flooding, 7 climbing film	22.2%
Co-current Flow (*climbing film* flow regime)	12	12 climbing film	100%

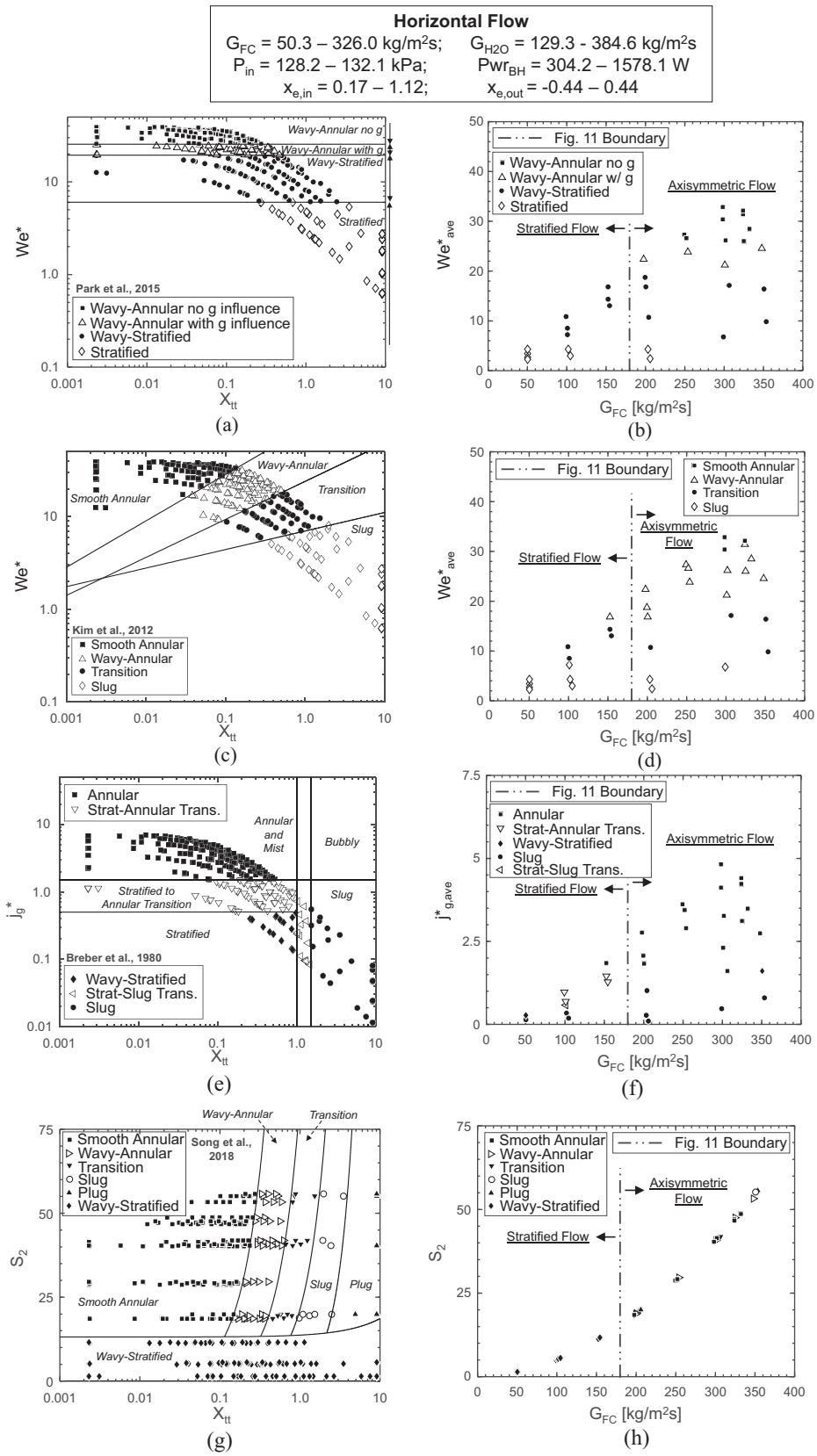

Fig. 10. Flow regime map of (a) Park et al. [36] used to evaluate current dataset, with (b) identified flow regimes across the range of mass velocities tested. Similar plots for flow regime maps of Kim et al. [40] (c), (d), Breber et al. [51] (e), (f), and Song et al. [60] (g), (h).

Table 4
Summary of flow regime identification approach in horizontal flow.

Experimentally identified flow regime	Number of experimentally determined cases	Predictions by Park et al. [36]	Percent correct	Predictions by Kim et al. [40]	Percent correct	Predictions by Breber et al. [51]	Percent correct	Predictions by Song et al. [60]	Percent correct
Stratified Flow (*stratified, wavy-stratified, plug* flow regimes)	12	6 stratified, 6 wavy-stratified	100%	7 slug, 4 transition, 1 wavy-annular	91.7%	5 slug, 1 wavy-stratified, 4 strat-annular transition,1 annular, 1 strat-slug	50.0%	12 wavy-stratified	100%
Axisymmetric Flow (*annular, wavy-annular, slug* flow regimes)	22	2 stratified, 7 wavy-stratified, 4 wavy-annular w/g, 9 wavy-annular no g	59.1%	3 slug, 4 transition, 12 wavy-annular, 3 smooth annular	68.2%	5 slug, 1 bubbly, 16 annular	100%	6 wavy-annular, 9 smooth annular, 5 plug, 1 slug, 1 transition	72.7%

Fig. 10(b) shows the predictions of Park et al.'s map (presented as 'channel average' flow regimes as was done in Fig. 9(c) for vertical upflow) as a function of mass velocity. For low FC-72 mass velocities, all cases are predicted to be either *stratified* or *wavy stratified* flow regime which matches well with the experimentally identified stratified flow boundary.

For higher mass velocity cases their map predicts a majority of cases will exhibit *annular flow* with a smaller number (primarily those cases with saturated mixture inlet conditions) still exhibiting *stratified flow* behavior.

Fig. 10(c) presents the map of Kim et al. [40] which relies on the same dimensionless groups proposed by Soliman [53,54]. Their work dealt with condensation of FC-72 inside a micro-channel heat sink, however, and they expressed their transition criteria as

$$\text{Smooth - annular to wavy - annular}: We^* = 90X_{tt}^{0.5}, \tag{18a}$$

$$\text{Wavy - annular to transition}: We^* = 24X_{tt}^{0.41}, \tag{18b}$$

$$\text{Transition to slug}: We^* = 7X_{tt}^{0.2}. \tag{18c}$$

Immediately apparent is that unlike the map of Park et al. [36], Kim et al. [40] expressed their transition criteria as a function of both We^* and X_{tt}. Due to the definition of X_{tt} in Eq. (15) showing a dependence on local fluid quality (as well as a combination of material properties), expressing regime transition criteria in terms of X_{tt} allows included effects of liquid content within the channel to be accounted for (*i.e.,* allowing differentiation between cases with low and high inlet qualities).

One added complexity when interpreting the map of Kim et al. is its lack of stratified flow regimes. Due to the original experimental work being micro-channel condensation and surface tension effects playing a dominant role in small-diameter channels, operating conditions which would provide stratified flow in larger diameter tubes are predicted to yield slug flow here. For the sake of the current analysis, cases where flow regime is predicted to be *slug flow* using the map of Kim et al. will be treated as representing stratified flow. This is not a bad assumption, as the original map is intended to show a transition from inertia dominated regimes (*i.e., annular flow*) to non-inertia dominated regimes (surface tension dominated in microchannels, gravity dominated in mini/macro-channels). It still represents an assumption, however, and care should be taken when utilizing this map for non-micro-channel flows.

Fig. 10(d) shows how predictions of channel average flow regime using the map of Kim et al. [40] change as mass velocity increases. For low mass velocity cases, most test cases are predicted to exhibit slug or transition flow, matching well with the experimental assessment of flow regime. For higher mass velocity cases, predictions are primarily of smooth-annular and wavy-annular flow, again matching well with experimental results outlined in Section 4. Similar to the map of Park et al. discussed above, however, is the prediction of non-inertia-dominated flow regimes for high mass velocities with saturated mixture inlet conditions.

The map of Breber et al. [51] is shown in Fig. 10(e). This map is one of the most commonly utilized flow regimes maps available for horizontal flow condensation and uses dimensionless superficial vapor velocity j_g^* and Lockhart-Martinelli parameter X_{tt} as its coordinates. They defined their transition criteria as

$$\text{Annular flow}: j_g^* > 1.5, X_{tt} < 1.0, \tag{19a}$$

$$\text{Wavy or stratified flow}: j_g^* < 0.5, X_{tt} < 1.0, \tag{19b}$$

$$\text{Slug flow}: j_g^* < 1.5, X_{tt} > 1.5, \tag{19c}$$

$$\text{Bubbly flow}: j_g^* > 1.5, X_{tt} > 1.5, \tag{19d}$$

with transition regimes between those explicitly defined above.

Investigation of flow regimes predicted using the map of Breber et al. [51] versus FC-72 mass velocity in Fig. 10(f) shows that, for low mass velocities, predicted regimes include *slug flow*, *wavy-stratified flow*, *stratified-annular transition*, *stratified-slug transition,* and even one case of *annular flow*. For high mass velocities, all but one case show *annular flow* and *slug flow* are predicted, however, both of which are axisymmetric regimes and match well with the experimentally identified behavior.

The final flow regime map presented is that of Song et al. [60] shown in Fig. 10(g), which has only recently become available in literature. Similar to other authors they use the Lockhart-Martinelli parameter X_{tt} as one of their dimensionless groups, but for the other group they define a new parameter S_2 as

$$S_2 = Fr_g Bd^{-0.15} Ca_f^{-0.1}\left(1 + Bo^{0.25}\right), \tag{20}$$

where vapor Froude number Fr_g, Bond number Bd, liquid Capillary number Ca_f, and modified Boiling number Bo are defined as

$$Fr_g = \frac{G^2}{\rho_g\left(\rho_f - \rho_g\right)gD}, \tag{21}$$

$$Bd = \frac{\left(\rho_f - \rho_g\right)gD^2}{\sigma}, \tag{22}$$

$$Ca_f = \frac{\mu_f G}{\rho_f \sigma}, \tag{23}$$

$$\text{and } Bo = \frac{Q_{cond}}{G_{FC} h_{fg}}. \tag{24}$$

They define their transition criteria as

$$\text{Wavy - stratified flow}: S_2 < (20 + X_{tt})^{0.86}, \tag{25a}$$

and if *wavy-stratified flow* is not present:

$$\text{Plug flow to slug flow}: S_2 = 2.45X_{tt}^{2.29}, \tag{25b}$$

$$\text{Slug flow to transition flow}: S_2 = 21.45X_{tt}^{1.71}, \tag{25c}$$

$$\text{Transition flow to wavy - annular flow}: S_2 = 83.4X_{tt}^{1.62}, \tag{25d}$$

$$\textit{and}\ \text{Wavy - annular flow to smooth - annular flow}: S_2 = 360.6X_{tt}^{1.52}. \tag{25e}$$

Fig. 10(h) shows the flow regime map of Song et al. [60] does an excellent job of predicting *wavy-stratified* flow for low mass velocities, as was seen when analyzing the experimental data. For high mass velocities, a mixture of *slug, plug, transition, wavy-annular,* and *smooth-annular* flow regimes is predicted, with the majority of cases predicted to be *smooth-annular*. Overall, the map of Song et al. does the best job of capturing experimental results out of all the maps presented here, evidenced by a 100% accuracy classifying stratified flow cases and 72.7% accuracy for axisymmetric flow shown in Table 4.

6. Conclusions

The present study investigated condensation flow regime in a smooth circular tube. Flow behavior as a function of condensate mass velocity in vertical upflow, vertical downflow, and horizontal flow orientations was assessed through flow visualization images. Qualitative trends were used as a starting point for development of a new methodology using temperature and pressure measurements to determine whether upflow condensation exhibited co-current or counter-current flow behavior (referring to liquid and vapor phases). Similarly, circumferentially spaced temperature measurements were used in horizontal flow to determine whether flow exhibited stratified or axisymmetric characteristics. The influence of interfacial waves on temperature fluctuations observed in vertical downflow condensation at low mass velocities was also discussed.

Experimentally determined flow regime boundaries were compared with results predicted by several popular flow regime maps for both vertical upflow and horizontal flow orientations. Assessments of their performances are provided in Tables 3 and 4 for upflow and horizontal orientations, respectively.

Key conclusions from this study are:

(1) Condensation flow regimes in vertical upflow may be grouped into those exhibiting co-current flow (*climbing film*) and those exhibiting counter-current flow (*flooding, oscillating film, falling film*). Similarly, horizontal flow regimes may be grouped as stratified (*stratified, wavy-stratified, plug*) and axisymmetric (*annular, slug, bubbly*).
(2) Liquid film behavior in vertical upflow condensation may be accurately determined as co-current or counter-current based on observed magnitudes of temperature and pressure fluctuations. If these fluctuations maintain the same amplitude or increase slightly as mass velocity is increased, flow is co-current. If they decrease as mass velocity increases, flow is counter-current.
(3) Liquid film distribution in horizontal flow condensation may be determined to be stratified or axisymmetric based on observed magnitudes of standard deviation between circumferentially spaced temperature measurements. If these values maintain the same magnitude or increase slightly as mass velocity is increased, flow is axisymmetric. If they decrease as mass velocity increases, flow is stratified.
(4) Comparison of identified flow regimes with those predicted by popular flow regime maps yield reasonable agreement across all maps investigated here. For vertical upflow, the map of Park and Mudawar [35] is capable of accurately predicting condensation flow regime. In horizontal flow the map of Song et al. [60] does the best job predicting flow regime.

Conflict of interest

The authors declared that there is no conflict of interest.

Acknowledgements

The authors are grateful for financial support provided by the National Aeronautics and Space Administration (NASA) under grant no. NNX17AK98G, and technical support of the NASA Glenn Research Center, Cleveland, Ohio. This work was also supported by NASA Space Technology Research Fellowship NNX15AP29H.

Appendix A. Supplementary material

Supplementary data to this article can be found online at https://doi.org/10.1016/j.ijheatmasstransfer.2019.01.133.

References

[1] I. Mudawar, Assessment of high-heat-flux thermal management schemes, IEEE Trans. – CPMT 24 (2001) 122–141.
[2] S. Lee, I. Mudawar, M.M. Hasan, Thermal analysis of hybrid single-phase, two-phase and heat pump thermal control system (TCS) for future spacecraft, Appl. Therm. Eng. 100 (2016) 190–214.
[3] F.P. Chiramonte, J.A. Joshi, Workshop on critical issues in microgravity fluids, transport, and reaction processes in advanced human support technology – final report, NASA TM-2004-212940, 2004.
[4] The National Academies, Recapturing a Future for Space Exploration: Life and Physical Sciences Research for a New Era, National Academies Press, Washington, DC, 2011.
[5] P.J. Marto, V.J. Lepere, Pool boiling heat transfer from enhanced surfaces to dielectric fluids, J. Heat Transfer 104 (1982) 292–299.
[6] I. Mudawar, T.M. Anderson, Parametric investigation into the effects of pressure, subcooling, surface augmentation and choice of coolant on pool boiling in the design of cooling systems for high-power density chips, J. Electronic Pack. 112 (1990) 375–382.
[7] D.E. Maddox, I. Mudawar, Single- and two-phase convective heat transfer from smooth and enhanced microelectronic heat sources in a rectangular channel, J. Heat Transfer 111 (1989) 533–542.
[8] I. Mudawar, D.E. Maddox, Enhancement of critical heat flux from high power microelectronic heat sources in a flow channel, J. Electronic Pack. 112 (1990) 241–248.
[9] C.O. Gersey, I. Mudawar, Effects of heater length and orientation on the trigger mechanism for near-saturated flow boiling critical heat flux – I. Photographic study and statistical characterization of the near-wall interfacial features, Int. J. Heat Mass Transf. 38 (1995) 629–641.
[10] J.C. Sturgis, I. Mudawar, Critical heat flux in a long, rectangular channel subjected to one-sided heating – I. Flow visualization, Int. J. Heat Mass Transf. 42 (1999) 1835–1847.
[11] J.C. Sturgis, I. Mudawar, Critical heat flux in a long, rectangular channel subjected to one-sided heating – II. Analysis of critical heat flux data, Int. J. Heat Mass Transf. 42 (1999) 1849–1862.
[12] S.M. Ghiaasiaan, Two-Phase Flow, Boiling and Condensation in Conventional and Miniature Systems, Cambridge University Press, New York, 2008.
[13] D.D. Hall, I. Mudawar, Ultra-high critical heat flux (CHF) for subcooled water flow boiling – II: high-CHF database and design equations, Int. J. Heat Mass Transf. 42 (1999) 1429–1456.
[14] T.J. LaClair, I. Mudawar, Thermal transients in a capillary evaporator prior to the initiation of boiling, Int. J. Heat Mass Transf. 43 (2000) 3937–3952.
[15] S. Mukherjee, I. Mudawar, Smart pumpless loop for micro-channel electronic cooling using flat and enhanced surfaces, IEEE Trans. – CPMT 26 (2003) 99–109.
[16] W. Qu, I. Mudawar, Thermal design methodology for high-heat-flux single-phase and two-phase micro-channel heat sinks, in: Proc. I-THERM 2002, San Diego, California, 2002, pp. 347–359.

[17] S. Mukherjee, I. Mudawar, Pumpless loop for narrow channel and micro-channel boiling from vertical surfaces, J. Electronic Pack. 125 (2003) 431–441.
[18] W. Qu, I. Mudawar, S.Y. Lee, S.T. Wereley, Experimental and computational investigation of flow development and pressure drop in a rectangular micro-channel, J. Electronic Pack. 128 (2005) 1–9.
[19] J. Lee, I. Mudawar, Critical heat flux for subcooled flow boiling in micro-channel heat sinks, Int. J. Heat Mass Transf. 52 (2009) 3341–3352.
[20] D.C. Wadsworth, I. Mudawar, Enhancement of single-phase heat transfer and critical heat flux from an ultra-high-flux simulated microelectronic heat source to a rectangular impinging jet of dielectric liquid, J. Heat Transfer 114 (1992) 764–768.
[21] M.E. Johns, I.I. Mudawar, An ultra-high power two-phase jet-impingement avionic clamshell module, J. Electronic Pack. 118 (1996) 264–270.
[22] W.P. Klinzing, J.C. Rozzi, I. Mudawar, Film and transition boiling correlations for quenching of hot surfaces with water sprays, J. Heat Treating 9 (1992) 91–103.
[23] D.D. Hall, I. Mudawar, Experimental and numerical study of quenching complex-shaped metallic alloys with multiple, overlapping sprays, Int. J. Heat Mass Transf. 38 (1995) 1201–1216.
[24] L. Lin, R. Ponnappan, Heat transfer characteristics of spray cooling in a closed loop, Int. J. Heat Mass Transf. 46 (2003) 3737–3746.
[25] M. Visaria, I. Mudawar, Effects of high subcooling on two-phase spray cooling and critical heat flux, Int. J. Heat Mass Transf. 51 (2008) 5269–5278.
[26] M. Visaria, I. Mudawar, Application of two-phase spray cooling for thermal management of electronic devices, IEEE Trans. – CPMT 32 (2009) 784–793.
[27] M.K. Sung, I. Mudawar, Experimental and numerical investigation of single-phase heat transfer using a hybrid jet impingement/micro-channel cooling scheme, Int. J. Heat Mass Transf. 49 (2006) 682–694.
[28] M.M. Chen, An analytical study of laminar film condensation: Part 2 – single and multiple horizontal tubes, J. Heat Transfer 83 (1961) 55–60.
[29] J.F. Roques, V. Dupont, J.R. Thome, Falling film transitions on plain and enhanced tubes, J. Heat Transfer 124 (2002) 491–499.
[30] Y.T. Kang, H. Hong, Y.S. Lee, Experimental correlation of falling film condensation on enhanced tubes with HFC134a; low-fin and Turbo-C tubes, Int. J. Refrig. 30 (2007) 805–811.
[31] M. Soliman, J.R. Schuster, P.J. Berenson, A general heat transfer correlation for annular flow condensation, J. Heat Transfer 90 (1968) 267–274.
[32] M.K. Dobson, J.C. Chato, Condensation in smooth horizontal tubes, J. Heat Transfer 120 (1998) 193–213.
[33] D. Jung, K. Song, Y. Cho, S. Kim, Flow condensation heat transfer coefficients of pure refrigerants, Int. J. Refrig. 26 (2003) 4–11.
[34] I. Park, S.M. Kim, I. Mudawar, Experimental measurement and modeling of downflow condensation in a circular tube, Int. J. Heat Mass Transf. 57 (2013) 567–581.
[35] I. Park, I. Mudawar, Climbing film, flooding and falling film behavior in upflow condensation in tubes, Int. J. Heat Mass Transf. 65 (2013) 44–61.
[36] I. Park, H. Lee, I. Mudawar, Determination of flow regimes and heat transfer coefficient for condensation in horizontal tubes, Int. J. Heat Mass Transf. 80 (2015) 688–716.
[37] X.R. Zhuang, G.F. Chen, H. Guo, Q.L. Song, Q.X. Tang, Z.Q. Yang, X. Zou, M.Q. Gong, Experimental investigation on flow condensation of zeotropic mixtures of methane/ethane in a horizontal smooth tube, Int. J. Refrig. 85 (2018) 120–134.
[38] C.-Y. Yang, H. Nalbandian, Condensation heat transfer and pressure drop of refrigerants HFO-1234yf and HFC-134a in small circular tube, Int. J. Heat Mass Transf. 127 (2018) 218–227.
[39] X. Quan, P. Cheng, H. Wu, Transition from annular flow to plug/slug flow in condensation of steam in microchannels, Int. J. Heat Mass Transf. 51 (2008) 707–716.
[40] S.M. Kim, J. Kim, I. Mudawar, Flow condensation in parallel micro-channels – Part 1: experimental results and assessment of pressure drop correlations, Int. J. Heat Mass Transf. 55 (2012) 971–983.
[41] S.M. Kim, I. Mudawar, Flow condensation in parallel micro-channels – Part 2: heat transfer results and correlation technique, Int. J. Heat Mass Transf. 55 (2012) 984–994.
[42] G. Liang, N. Mascarenhas, I. Mudawar, Analytical and experimental determination of slug flow parameters, pressure drop and heat transfer coefficient in micro-channel condensation, Int. J. Heat Mass Transf. 111 (2017) 1218–1233.
[43] M.A. Vanderputten, T.A. Jacob, M. Sattar, N. Ali, B.M. Fronk, Two-phase flow regimes of condensing R-134a at low mass flux in rectangular microchannels, Int. J. Refrig. 84 (2017) 92–102.
[44] J. Wang, J.M. Li, Theoretical and experimental study of wavy flow during R134a condensation flow in symmetrically and asymmetrically cooled microchannels, Int. J. Multiph. Flow 101 (2018) 125–136.
[45] A. Umur, P. Griffith, Mechanism of dropwise condensation, J. Heat Transfer 87 (1965) 275–282.
[46] J.W. Rose, L.R. Glicksman, Dropwise condensation – the distribution of drop sizes, Int. J. Heat Mass Transf. 16 (1973) 411–425.
[47] X. Chen, M.M. Derby, Droplet departure modeling and a heat transfer correlation for dropwise flow condensation in hydrophobic min-channels, Int. J. Heat Mass Transf. 125 (2018) 1096–1104.
[48] G.B. Wallis, Flooding velocities for air and water in vertical tubes, No. AEEW-R-123, United Kingdom Atomic Energy Authority, Reactor Group, Atomic Energy Establishment, Winfrith, Dorset, England, 1961.
[49] Y. Taitel, A.E. Dukler, A model for predicting flow regime transitions in horizontal and near horizontal gas-liquid flow, AIChE J. 22 (1976) 47–55.
[50] J.M. Mandhane, G.A. Gregory, K. Aziz, A flow pattern map for gas-liquid flow in horizontal pipes, Int. J. Multiph. Flow 1 (1974) 537–553.
[51] G. Breber, J.W. Palen, J. Taborek, Prediction of horizontal tubeside condensation of pure components using flow regime criteria, J. Heat Transfer 102 (1980) 471–476.
[52] T.N. Tandon, H.K. Varma, C.P. Gupta, A new flow regimes map for condensation inside horizontal tubes, J. Heat Transfer 104 (1982) 763–768.
[53] H.M. Soliman, On the annular-to-wavy flow pattern transition during condensation inside horizontal tubes, Can. J. Chem. Eng. 60 (1982) 475–481.
[54] H.M. Soliman, The mist-annular transition during condensation and its influence on the heat transfer mechanism, Int. J. Multiph. Flow 12 (1986) 277–288.
[55] Q. Chen, R.S. Amano, M. Xin, Experimental study of flow patterns and regimes of condensation in horizontal three-dimensional micro-fin tubes, Heat Mass Transf. 43 (2006) 201–206.
[56] A. Cavallini, G. Censi, D. Del Col, L. Doretti, G.A. Longo, L. Rossetto, In-tube condensation of halogenated refrigerants, ASHRAE Trans. 108 (2002) 146–161.
[57] W.W.W. Wang, T.D. Radcliff, R.N. Christensen, A condensation heat transfer correlation for millimeter-scale tubing with flow regime transition, Exp. Therm. Fluid Sci. 26 (2002) 473–485.
[58] J. El Hajal, J.R. Thome, A. Cavallini, Condensation in horizontal tubes, part 1: two-phase flow pattern map, Int. J. Heat Mass Transf. 46 (2003) 3349–3363.
[59] J.W. Coleman, S. Garimella, Two-phase flow regimes in round, square, and rectangular tubes during condensation of refrigerant R134a, Int. J. Refrig. 26 (2003) 117–128.
[60] Q. Song, G. Chen, Z. Yang, H. Wang, M. Gong, New adiabatic and condensation two-phase flow pattern maps of R14 in a horizontal tube, Int. J. Heat Mass Transf. 127 (2018) 910–924.
[61] L. Liebenberg, J.R. Thome, J.P. Meyer, Flow visualization and flow pattern identification with power spectral density distributions of pressure traces during refrigerant condensation in smooth and microfin tubes, J. Heat Transfer 127 (2005) 209–220.
[62] L. Liebenberg, J.P. Meyer, The characterization of flow regimes with power spectral density distributions of pressure fluctuations during condensation in smooth and micro-fin tubes, Exp. Therm. Fluid Sci. 31 (2006) 127–140.
[63] I. Mudawar, Flow boiling and flow condensation in reduced gravity, Adv. Heat Transfer 49 (2017) 225–306.
[64] H. Zhang, I. Mudawar, M.M. Hasan, Experimental assessment of the effects of body force, surface tension force, and inertia on flow boiling CHF, Int. J. Heat Mass Transf. 45 (2002) 4079–4095.
[65] H. Zhang, I. Mudawar, M.M. Hasan, Flow boiling CHF in microgravity, Int. J. Heat Mass Transf. 48 (2005) 3107–3118.
[66] C. Konishi, I. Mudawar, Review of flow boiling and critical heat flux in microgravity, Int. J. Heat Mass Transf. 80 (2015) 469–493.
[67] H. Lee, I. Mudawar, M.M. Hasan, Flow condensation in horizontal tubes, Int. J. Heat Mass Transf. 66 (2013) 31–45.
[68] H. Lee, I. Park, C. Konishi, I. Mudawar, R.L. May, J.R. Juergens, J.D. Wagner, N.R. Hall, H.K. Nahra, M.M. Hasan, J.R. Mackey, Experimental investigation of flow condensation in microgravity, J. Heat Transfer 136 (2013) 021502.
[69] I. Park, L.E. O'Neill, C.R. Kharangate, I. Mudawar, Assessment of body force effects in flow condensation, Part I: experimental investigation of liquid film behavior for different orientations, Int. J. Heat Mass Transf. 106 (2017) 295–312.
[70] L.E. O'Neill, I. Park, C.R. Kharangate, V.S. Devahdhanush, V. Ganesan, I. Mudawar, Assessment of body force effects in flow condensation, part II: criteria for negating the influence of gravity, Int. J. Heat Mass Transf. 106 (2017) 313–328.
[71] H. Lee, C.R. Kharangate, N. Mascarenhas, I. Park, I. Mudawar, Experimental and computational investigation of vertical downflow condensation, Int. J. Heat Mass Transf. 85 (2015) 865–879.
[72] C.R. Kharangate, H. Lee, I. Park, I. Mudawar, Experimental and computational investigation of vertical upflow condensation in a circular tube, Int. J. Heat Mass Transf. 95 (2016) 249–263.
[73] L.E. O'Neill, I. Mudawar, M.M. Hasan, H.K. Nahra, R. Balasubramaniam, J.R. Mackey, Flow condensation pressure oscillations at different orientations, Int. J. Heat Mass Transf. 127 (2018) 784–809.
[74] S.M. Kim, I. Mudawar, Universal approach to predicting two-phase frictional pressure drop for adiabatic and condensing mini/micro-channel flows, Int. J. Heat Mass Transf. 55 (2012) 3246–3261.
[75] S.M. Kim, I. Mudawar, Universal approach to predicting heat transfer coefficient for condensing mini/micro-channel flow, Int. J. Heat Mass Transf. 56 (2013) 238–250.
[76] S.M. Kim, I. Mudawar, Review of databases and predictive methods for heat transfer in condensing and boiling mini/micro-channel flows, Int. J. Heat Mass Transf. 77 (2014) 627–652.
[77] S.M. Kim, I. Mudawar, Review of databases and predictive methods for pressure drop in adiabatic, condensing and boiling mini/micro-channel flows, Int. J. Heat Mass Transf. 77 (2014) 74–97.
[78] C.R. Kharangate, I. Mudawar, Review of computational studies on boiling and condensation, Int. J. Heat Mass Transf. 108 (2017) 1164–1196.
[79] L.E. O'Neill, R. Balasubramaniam, H.K. Nahra, M.M. Hasan, I. Mudawar, Flow condensation heat transfer in a smooth tube at different orientations: Experimental results and predictive models, Int. J. Heat Mass Transf. (in preparation).

[80] L.E. O'Neill, C.R. Kharangate, I. Mudawar, Time-averaged and transient pressure drop for flow boiling with saturated inlet conditions, Int. J. Heat Mass Transf. 103 (2016) 133–153.
[81] L.E. O'Neill, I. Mudawar, M.M. Hasan, H.K. Nahra, B. Ramaswamy, N.R. Hall, A. Lokey, J.R. Mackey, Experimental investigation into the impact of density wave oscillations on flow boiling system dynamic behavior and stability, Int. J. Heat Mass Transf. 120 (2018) 144–166.
[82] L.E. O'Neill, I. Mudawar, Mechanistic model to predict frequency and amplitude of density wave oscillations in vertical upflow boiling, Int. J. Heat Mass Transf. 123 (2018) 143–171.
[83] L.E. O'Neill, I. Mudawar, M.M. Hasan, H.K. Nahra, B. Ramaswamy, J.R. Mackey, Experimental investigation of frequency and amplitude of Density Wave Oscillations in vertical upflow boiling, Int. J. Heat Mass Transf. 125 (2018) 1240–1263.
[84] J.R. Thome, J. El Hajal, A. Cavallini, Condensation in horizontal tubes, part 2: new heat transfer model based on flow regimes, Int. J. Heat Mass Transf. 46 (2003) 3365–3387.
[85] M.M. Shah, An improved and extended general correlation for heat transfer during condensation in plain tubes, HVAC&R Res. 15 (2009) 889–913.
[86] J.P. Meyer, D.R.E. Ewim, Heat transfer coefficients during the condensation of low mass fluxes in smooth horizontal tubes, Int. J. Multiph. Flow 99 (2018) 485–499.
[87] Y. Camaraza-Medina, A. Hernandez-Guerrero, J.L. Luviano-Ortiz, K. Mortensen-Carlson, O.M. Cruz-Fonticiella, O.F. Garcia-Morales, New model for heat transfer calculation during film condensation inside pipes, Int. J. Heat Mass Transf. 128 (2019) 344–353.
[88] P.L. Kapitza, S.P. Kapitza, Wave flow in thin layers of a viscous fluid, Zh. Exper. Teor Fiz. 19 (1949) 105.
[89] V. Balakotaiah, S.S. Jayawardena, Stability of wavy films in gas-liquid two-phase flows at normal and microgravity conditions, in: Third Microgravity Fluid Physics Conf., 1996, pp. 103–108.
[90] N. Nusselt, Die oberflachenkondensation des wasserdampfes, Z. Ver. Dt. Ing. 60 (1916) 541–569.
[91] T. Ueda, T. Tanaka, Studies of liquid film flow in two-phase annular and annular-mist flow regions (Part 1, downflow in a vertical tube), Bull. JSME 17 (1974) 603–613.
[92] I.A. Mudawwar, M.A. El-Masri, Momentum and heat transfer across freely-falling turbulent liquid films, Int. J. Multiph. Flow 12 (1986) 771–790.
[93] T.H. Lyu, I. Mudawar, Statistical investigation of the relationship between interfacial waviness and sensible heat transfer to a falling liquid film, Int. J. Heat Mass Transf. 34 (6) (1991) 1451–1464.
[94] A. Miyara, Numerical analysis on flow dynamics and heat transfer of falling liquid films with interfacial waves, Heat Mass Transf. 35 (1999) 298–306.